Armadillo repeat-containing kinesin represents the versatile plus-end-directed transporter in Physcomitrella

Mari W. Yoshida[1], Maya Hakozaki [1], and Gohta Goshima[1,2*]

1. Department of Biological Science, Graduate School of Science, Nagoya University, Nagoya 464-8602, Japan

2. Sugashima Marine Biological Laboratory, Graduate School of Science, Nagoya University, Toba 517-0004, Japan

*To whom correspondence should be addressed. Email: goshima@bio.nagoya-u.ac.jp

Author contributions: M.W.Y. and G.G. designed the research; M.W.Y. performed the experiments and analysed the data; M.W.Y. and M.H. selected the transgenic lines; M.W.Y. and G.G. wrote the paper.

Abstract

Kinesin-1, also known as conventional kinesin, is widely utilised for microtubule plus-end-directed ("anterograde") transport of various cargos in animal cells. However, a motor functionally equivalent to the conventional kinesin has not been identified in plants, which lack the kinesin-1 genes. Here, we show that plant-specific armadillo repeat-containing kinesin (ARK) is the long sought-after versatile anterograde transporter in plants. In *ARK* mutants of the moss *Physcomitrium patens*, the anterograde motility of nuclei, chloroplasts, mitochondria, and secretory vesicles was suppressed. Ectopic expression of non-motile or tail-deleted ARK did not restore organelle distribution. Another prominent macroscopic phenotype of *ARK* mutants was the suppression of cell tip growth. We showed that this defect was attributed to the mislocalisation of actin regulators, including RopGEFs; expression and forced apical localisation of RopGEF3 suppressed the growth phenotype of the *ARK* mutant. The mutant phenotypes were partially rescued by ARK homologues in *Arabidopsis thaliana*, suggesting the conservation of ARK functions in plants.

Key words

Kinesin/Microtubule-based transport/Cell tip growth/Actin/*Physcomitrium (Physcomitrella) patens*

Introduction

The proper positioning of cellular components in the cytoplasm is critical for cell physiology. It is particularly important for highly polarised cells, such as neurons and epithelial cells, in animals. Regulated bidirectional transport on microtubules is a major mechanism for positioning intracellular components and requires motor proteins that bind to cargo and walk on microtubules [1–3]. In animal cells, cytoplasmic dynein is responsible for the majority of minus-end-directed (retrograde) transport in the cytoplasm, and a few kinesin family members have been identified as plus end-directed (anterograde) transporters [1]. Among them, kinesin-1, also called conventional kinesin, is a universal transporter whose critical roles have been identified in various cell types [4–6]. Cargos of kinesin-1 include giant organelles, such as nuclei and mitochondria, as well as smaller

cellular components, such as secretory vesicles, protein complexes, and RNA granules [7–11]. These anterograde and retrograde transporters work together on the same cargo to allow bidirectional transport [12,13].

Intriguingly, plants do not possess cytoplasmic dynein or conventional kinesin. Intracellular transport in plants has long been believed to be predominantly driven by myosin and actin. Cytoplasmic streaming is the best-studied phenomenon observed in many plant cell types and is powered by myosin motors [14,15]. Furthermore, in *Arabidopsis thaliana* root hair, myosin XI-i transports the nucleus to the centre of the growing cell [16]. Chloroplast photo-relocation, a phenomenon in which chloroplasts are repositioned in response to light stimuli, is also promoted by specific chloroplast-associated actin filaments that polymerise between the plasma membrane and the chloroplasts in *A. thaliana* [17]. However, the microtubule-dependent motility of cellular components also exists in plants. For example, nuclear movement requires microtubules in several organisms and tissues. In tobacco BY-2 cells, microtubules and kinesins with the calponin-homology domain (KCH) are involved in nuclear positioning [18–20]. Microtubule-dependent nuclear positioning also occurs in meristemoid mother cells of *A. thaliana* and *Nicotiana tabacum* microspores [21,22]. In the former case, nuclear positioning affected stomatal patterning, suggesting the physiological importance of microtubule-dependent nuclear migration. A series of studies using protonemal tissue of the moss *Physcomitrium patens* (formerly called *Physcomitrella patens*) have also revealed the contribution of microtubules and motors to organelle transport. The tip-growing apical cell of *P. patens* protonema is an ideal system for studying microtubule-dependent bidirectional transport, as ~90% of the microtubules are oriented in such a manner that the plus ends face the cell tip during interphase [23]. In this system, when plus-end-directed motility is predominant over minus-end-directed motility, the organelle moves apically and is abundant on the apical side, and vice versa. Based on this advantage, several kinesin-14 family members have been identified as the drivers of retrograde transport, namely KCH for the nucleus, KCBP for the chloroplast and telophase chromosome, and ATK for newly formed microtubules [24–26]. Studies in *P. patens* thus drew a functional analogy between kinesin-14s and dynein and further illustrated the contribution of intracellular transport driven by the microtubule-kinesin mechanism.

Anterograde transporter is a missing piece in the model of intracellular transport in plants. Plant genomes do not encode proteins paralogous to kinesin-1, which is characterised by a unique domain in its tail that binds to the light chain [27]. Kinesin-3 is another potent cargo transporter in animal cytoplasm, and it is best known as a synaptic vesicle transporter in neurons [28,29]. However, this subfamily is also missing in plants; thus, no deduction can be made from genome sequences regarding the identity of the versatile anterograde transporter in plants. Nevertheless, Armadillo repeat-containing kinesin (ARK), which constitutes a subfamily unique to the plant lineage, could be a candidate motor protein. In a previous study, we observed that the nucleus was not properly positioned after inducing RNAi that targeted two of the four *ARK* genes in moss protonemata [30]. However, whether ARK is a genuine transporter of the nucleus could not be clarified. Although the purified ARKb motor can glide microtubules in the conventional *in vitro* gliding assay (i.e. motor activity is present), the motility of ARKb-Citrine on the microtubules *in vivo* could not be observed [30]. This contrasts with the observation that retrograde transporters show fast (~400 nm/s) and long (~1 μm) minus

end-directed motility *in vivo* [24,31]. Furthermore, AtARK1, the most-studied ARK, is localised to the plus end of microtubules, triggers microtubule catastrophe [32], and tethers the ER to the microtubule end by binding to the ER-shaping protein atlastin GTPase RHD3 [33]. Alterations in microtubule dynamics can, in principle, affect nuclear motility, as shown in yeast [34]. However, none of these previous studies have clarified the mechanism by which ARK positions nuclei.

This study initially aimed to elucidate how ARK proteins position the nuclei. Surprisingly, in the newly established *ARK* mutant lines, microtubule plus-end-directed motility of not only the nuclei but also chloroplasts, mitochondria, and secretory vesicles was suppressed. ARK was enriched around the nucleus in a tail-dependent but motor-independent manner, and non-motile or tail-deleted ARK did not restore organelle distribution. ARKb is a processive motor according to a single motor motility assay *in vitro*. Furthermore, when a brighter fluorescent protein, mNeonGreen (mNG), was attached to the endogenous ARKb, processive motility towards the microtubule plus ends was observed also *in vivo*. The most prominent macroscopic phenotype of *ARK* mutants was the suppression of cell tip growth, which is known to require the actin cytoskeleton. Interestingly, this defect was attributed to the mislocalisation of actin regulators, including the guanine nucleotide exchange factors (GEFs) of Rho-type GTPases. These phenotypes were partially rescued by the ectopic expression of ARK homologues in *A. thaliana*. These results suggest that ARK is a versatile anterograde transporter in Physcomitrella and possibly transports cargo in other plant species.

Results

P. patens ARK is required for protonemal growth

Four highly homologous genes are present in the ARK family of *P. patens* [35,36]. Previously, we examined the RNAi knockdown mutant of *ARK* and identified a specific defect in protonemal apical cells, namely, nuclear mispositioning [30]. The RNAi targeted *ARKa* and *ARKb* genes and reduced their mRNA levels by ~50%, whereas ARKc and ARKd were kept intact, which might have prevented the expression of several potential phenotypes. To isolate multiple loss-of-function mutants of *ARK*, we used CRISPR/Cas9. We attempted to simultaneously introduce a frameshift just before the critical, conserved ATPase motif or microtubule-binding site in the motor domain of *ARKa-d*, which would destroy its motor activity [37–39]. We used two parental lines, which expressed mCherry-α-tubulin and GFP-α-tubulin/Histone2B-mCherry. Consequently, we obtained independent mutants containing a variety of mutations in different gene sets from both backgrounds (Table S1). Overall, all the isolated single- and double frame-shifted lines (*a*, *b*, *ab*, *ad*, *bc*, and *bd*) showed no or only mild growth defects (Fig. S1A). In contrast, the plant area of the triple (*abc*) and quadruple (*abcd*) mutants were dramatically smaller than those of the parental line (Fig. 1A, B). One line, called *ARKabcd-1*, possessed frameshift mutations in all the *ARK* genes (GFP-α-Tubulin/Histone2B-mCherry background), whereas the other, *ARKabc-1*, had deletions in *ARKa*, *ARKb*, and *ARKc*, but *ARKd* remained intact (mCherry-α-tubulin background) (Fig. S1B, Table S1). These two lines were chosen for further analyses.

The protonemal tissue was underdeveloped in *ARKabc-1* and *ARKabcd-1* (Fig. 1A, top and second rows). The phenotype was more severe in *ARKabcd-1* than *ARKabc-1*,

135 and gametophore tissue (leafy shoot) predominated on the culture medium (Fig. 1A, top
136 row). The morphology of the *ARKabc-1* gametophore was normal, but twisted phyllids
137 (leaf-like tissue) consisting of abnormally shaped cells were observed in *ARKabcd-1* (Fig.
138 1A, third and fourth rows). In addition, *ARKabc-1* and *ARKabcd-1* developed fewer and
139 shorter rhizoids (root-like filamentous outgrowths) than the parental lines (Fig. S1C, D).
140 To confirm that the observed phenotype was derived from the disruption of the *ARK*
141 genes, we performed a rescue experiment in which the ARKb-mNeonGreen (mNG)
142 transgene was ectopically expressed in the mutants. We failed to transform the construct
143 into *ARKabcd-1* in multiple attempts; sufficient numbers of viable protoplasts for
144 transformation could not be obtained from this extremely unhealthy line. In contrast,
145 *ARKabc-1* was transformable and a transgenic line stably expressing ARKb-mNG was
146 established. The plant growth of this line was restored, indicating that the protonemal
147 growth defect was caused by a reduction in ARK protein levels (Fig. 1A, B, S1C, D). To
148 determine whether the growth defect was associated with the motor activity of ARKb, we
149 constructed a "rigor" mutant of ARK (ARKb (T169N) -mNG), which binds to
150 microtubules but does not show motility [40]. We observed that the growth of protonema
151 or rhizoids was not rescued by the expression of this mutant ARK (Fig. 1A, B, S1C, D).
152 These results indicate that ARKs with intact motor activity are, likely redundantly,
153 required for protonemal and rhizoid growth as well as gametophore development.
154

155 **ARK is required for intracellular transport of the nucleus, chloroplast,**
156 **mitochondrion, and secretory vesicle**

157 We next performed time-lapse fluorescence microscopy on the *ARK* mutants,
158 focusing on nuclear motility. The underdevelopment of the protonemal tissue prevented
159 us from imaging and analysing the long-distance motility of organelles in *ARKabcd-1*.
160 Therefore, *ARKabc-1* which showed less severe protonemal growth defects, was used for
161 the cellular analysis. Consistent with the results of a study using *ARKa*/*b* RNAi [30], the
162 nucleus moved basally after anaphase and was located adjacent to the basal cell wall in
163 the apical cells of *ARKabc-1* (Fig. 2A, B; nuclei can be identified as an area devoid of
164 mCherry-α-tubulin signals in each z-slice). Like the control cells, the mispositioned
165 nuclei in the mutant cells also showed apical movement during mitotic prophase (Fig. 2B;
166 -60~0 min). However, because of the overly basal localisation of the nucleus during
167 interphase, mitotic spindle formation occurred more basally than in the control line (Fig.
168 2C). The mispositioning of the spindle was more drastic than that observed in the previous
169 *ARKa*/*b* RNAi line [30], suggesting that the previous RNAi line represented a weaker
170 hypomorphic allele. Importantly, the position of the nucleus and spindle was largely
171 rescued by ectopic expression of ARKb-mNG but not by that of the rigor mutant,
172 indicating that the nuclear mispositioning was associated with the loss of ARK motor
173 activity (Fig. 2A–C).
174 The constant, rapid, and bidirectional motility of chloroplasts during the normal cell
175 cycle is dependent on microtubules, and KCBP kinesin (kinesin-14VI) drives their
176 retrograde transport [25]. However, the factor(s) responsible for anterograde movement (i.e.
177 plus-end-directed transporters) remains unknown. During imaging, we realised that
178 chloroplasts in the mutant behaved differently from those in the control line. In *ARKabc-*
179 *1*, chloroplasts moved basally overall and clustered near the basal cell wall in the apical
180 cell (Fig. 2A, D, E, Movie 1). This behaviour was opposite to that of the *KCBP* knockout

181 line, in which chloroplasts were predominantly moved to and observed on the apical side
182 of the cell [25]. This phenotype was also rescued by ectopic expression of ARKb-mNG but
183 not by the rigor mutant (Fig. 2A, E). These results indicate that the bidirectional motility
184 of the chloroplast is driven by KCBP (retrograde) and ARK (anterograde).
185 To the best of our knowledge, ARK is the first anterograde kinesin to be identified
186 as a participant in the movement of multiple organelles in plant cells. This led us to
187 hypothesise that ARK may be a versatile anterograde motor for many cargos, similar to
188 conventional kinesin in animals. To test this possibility, we analysed the mitochondrion,
189 another giant membranous organelle possessing DNA. To visualise the mitochondria, the
190 mitochondrial membrane protein γ-F1ATPase-mNG was expressed in *ARKabc-1* and the
191 control lines. Mitochondria showed bidirectional movement along cytoplasmic
192 microtubules (Fig. 2G, Movie 2); however, most of them translocated apically from their
193 initial positions in the control line after tracking for 6 min (65 of 72 mitochondria in 12
194 cells; Fig. 2H). In contrast, more basal translocation was observed in *ARKabc-1* (38 of 72
195 mitochondria in 12 cells). Ectopic ARKb-mNG expression in the mutant largely restored
196 apically directed preference (58 of 72 mitochondria in 12 cells). The overall
197 mitochondrial distribution in the control and *ARKabc-1* mutants were similar; the
198 mitochondria were distributed throughout the cytoplasm with modest apical enrichment
199 in most cells (Fig. 2F) [41]. However, apical enrichment was scarcely observed when *ARKd*
200 was deleted in *ARKabc-1* mutant (12 out of 14 cells showed no accumulation; Fig. 2F).
201 These results suggest that ARK is involved in the plus-end-directed transport of
202 mitochondria.
203 Next, we focused on secretory vesicles, which are also known cargos of kinesin-1
204 and kinesin-3 in animals [1]. In *P. patens,* actin-based motor myosin XI transports RabE14-
205 positive vesicles near the cell apex [42]. Whether microtubules and kinesins are involved in
206 vesicle transport remains unknown. Referring to the literature on *Arabidopsis* [43], we
207 labelled vesicles by tagging endogenous RabA2b with mNG in the control and *ARKabc-*
208 *1* lines. RabA2b is a small GTPase homologous to Rab-A2 in *A. thaliana*, which regulates
209 the secretory pathway by recruiting SNARE proteins [44]. In the control line, the mNG-
210 RabA2b signal accumulated at the apex (Fig. 3A). Time-lapse imaging using a spinning-
211 disc confocal microscope identified motile small puncta (Movie 3). When we focused on
212 long-distance movement of the puncta toward the cell tip (i.e. plus-end-directed motility),
213 we observed that it was markedly suppressed when the microtubules or actin were
214 depolymerised by latrunculin A or oryzalin (Fig. 3C). Thus, both actin- and microtubule-
215 dependent mechanisms are responsible for the long-range transport of RabA2b-
216 containing vesicles. In *ARKabc-1,* the number of long-distance movements of mNG-
217 RabA2b slightly decreased, whereas ectopic expression of ARKb-mNG restored motility
218 (Fig. 3D). Consistent with these observations, the RabA2b signal at the apex was smaller
219 in *ARKabc-1* than the control line (Fig. 3A, B, Movie 4). These results suggest that ARK
220 is involved in the microtubule plus-end-directed transport of RabA2b-containing vesicles,
221 in addition to giant organelles.
222
223 **Microtubule polymerisation dynamics are unaltered in the absence of ARK in moss**
224 *Arabidopsis* ARK1 promotes microtubule catastrophe in root hair cells [32]. We
225 examined whether alterations in microtubule polymerisation dynamics underlie the *ARK*
226 mutant phenotypes. To this end, we used oblique illumination fluorescence microscopy

227 to trace individual microtubule ends in protonemal apical cells [45]. However, most of the
228 parameters of microtubule dynamics, including catastrophe frequency, were not
229 significantly altered in *ARKabc-1* or *ARKabcd-1* (Fig. S2A, Movie 5, Table S2). For
230 example, the growth rate was slightly increased in *ARKabc-1* but not in *ARKabcd-1*.
231 Microtubule orientation near the cell tip was further analysed through tracing EB1-
232 Citrine, which binds to the growing ends of microtubules. Similarly, drastic difference
233 was not detected between *ARKabc-1* and control (Fig. S2B). Thus, the observed
234 phenotype of the mutants is unlikely to be due to the misregulation of polymerisation
235 dynamics or the misorientation of the microtubules.
236
237 **ARK shows processive, plus-end-directed motility**
238 Although endogenous ARKs labelled with Citrine were localised to the microtubules,
239 directional movement was not detected in a previous study [30]. However, the observed lack
240 of motility might have been due to the insufficient sensitivity of the microscopy, which
241 could not detect a single Citrine molecule [46]. In the present study, the brighter fluorescent
242 protein mNG [47] was used to label endogenous ARKb and its localisation was revisited.
243 Consistent with the previous study, ARKb-mNG was observed on microtubules. Most of
244 them were dissociated from microtubules without showing motility (Fig. 4A, C, Movie
245 6). Interestingly, however, some small punctate signals moved along the microtubules at
246 572 ± 243 nm/s (velocity, ±SD) for 986 ± 416 nm (run length, ±SD) (Fig. 4B–D). These
247 values are comparable to those of retrograde transporters (kinesin-14s) in moss (KCBPb,
248 ~413 nm/s, ~1.0 µm: KCHa, ~441 nm/s, ~1.6 µm) [24,31] but much faster than microtubule
249 growth (<100 nm/s; Fig. S2A). In contrast, no movement was observed in the rigor mutant
250 ARKb (T169N) -mNG (Fig. 4C).
251 Next, the dimeric motor construct was purified (ARKb [1–613 aa]-GFP; Fig. 4E) and
252 mixed with microtubules *in vitro*. In this assay, each punctate GFP signal represents a
253 single motor. We observed GFP puncta that exhibited directional motility along
254 microtubules (Movie 7). The motility rate was 340 ± 138 nm/s (±SD) and run length was
255 3.13 ± 2.17 µm (±SD) (Fig. 4F–H). Thus, ARKb is a processive motor. Together with the
256 *in vivo* assay data, these results suggest that moss ARK is capable of transporting cargo.
257 To evaluate the relevance of the observed ARKb velocity in cargo transport, we
258 measured the organelle motility rate. For the nucleus and chloroplast, we used *KCH*Δ and
259 *KCBP*Δ lines, respectively, to eliminate retrograde motility and possible counteracting
260 forces acting on the organelles [24,25]. The rates were negatively correlated with the
261 organelles size (Fig. S3). The motility of the nucleus (11.1 ± 6.49 nm/s, ±SD) was an
262 order of magnitude lower than the mean velocity of ARKb motor *in vitro*, whereas apical
263 mitochondria motility (219 ± 110 nm/s, ±SD) was more comparable to the ARKb motility
264 observed *in vitro* and *in vivo*. The motility rate of small RabA2b-marked vesicles,
265 although showing a broad range because the actin-based mechanism likely co-opted (Fig.
266 3C), overlapped with the range of ARKb motility observed *in vivo*. Overall, the results
267 are consistent with the known cargo size–velocity relationship of intracellular transport
268 [48,49], and support the model that ARK acts as an intracellular transporter of multiple
269 organelles.
270
271 **Tail region of ARK is required for organelle distribution and protonemal growth**
272 ARK family kinesins are distinguished from other kinesins by the presence of an

273 armadillo (ARM) repeat in the tail region, which is known as a protein-protein interaction
274 motif [50]. The ARM domain in the tail region is dispensable for AtARK1 to regulate
275 microtubule catastrophe [51]. However, if ARK is a cargo transporter, the tail would be a
276 potential cargo-binding site. To test whether the tail is required for ARK functions, two
277 deletion constructs were transformed into *ARKabc-1* (Fig. S4A). Interestingly, the
278 constructs lacking ARM (ΔARM, ΔTail) failed to rescue protonemal tissue growth or the
279 position of the chloroplasts (Fig. S4B, C, Movie 8). Thus, not only motor activity, but
280 also ARM, is indispensable for ARK function in moss.
281 Next, we expressed only the tail region (i.e. headless ARK) tagged with mNG in
282 mCherry-tubulin-expressing moss. The mNG signal was detected in the cytoplasm. In
283 addition, it was enriched around the nucleus, suggesting that the tail can interact with the
284 cargo nucleus independent of microtubules (Fig. 4I). Consistent with this notion, full-
285 length ARKb, but not tail-deleted ARKb (ΔTail), accumulated at the nuclear surface after
286 microtubule depolymerisation with oryzalin (Fig. 4J). Furthermore, headless ARK
287 expression caused mispositioning of the nucleus after cell division, phenocopying the
288 *ARKabc-1* mutant (Fig. 4K). The appearance of a dominant-negative effect suggests that
289 ARK interacts with its cargo via its tail region.
290
291 **ARK enables polarised cell growth by localising RopGEF to the cell tip**
292 A prominent phenotype associated with *ARK* deletion is the suppression of
293 protonemal tissue growth (Fig. 1). At the cellular level, we observed that the protonemal
294 apical and subapical cells were shorter in the mutants than the control line (Fig. 5A, B).
295 One possible explanation for this phenotype is the shortening of the cell cycle (i.e.
296 precocious entry into the M-phase) [52]. However, this was not the case, because the
297 duration of the cell cycle was unchanged between the two rounds of mitosis in *ARKabc-*
298 *1* (Fig. S5A). Instead, tip elongation significantly slowed in *ARKabc-1*, which was
299 consistent with the prevalence of shorter cells (Fig. 5C). Furthermore, protonemal cells
300 in *ARKabcd-1* exhibited round morphology, suggesting that cell polarity was disturbed
301 (Fig. 5A, right). To analyse this phenotype in more detail, we introduced an inducible
302 RNAi construct targeting *ARKd* into *ARKabc-1* and observed tip growth upon RNAi
303 induction. Unlike the *ARKabcd-1* cells, the protonemal cells of this line were rod-shaped
304 before RNAi induction, such that the requirement of ARK for polarised growth could be
305 directly assessed by time-lapse imaging after RNAi induction. We observed that the
306 protonemal cells frequently produced multiple tips in the RNAi line (Fig. S6A, B, Movie
307 9).
308 The slowing or suppression of tip growth in protonemal cells is reminiscent of the
309 results of actin dysfunction (confirmed in Fig. S5B) [53,54]. Indeed, F-actin foci at the cell
310 apex, which ensure rapid tip growth [55], were less frequently observed in the absence of
311 *ARKabc-1* (Fig. 5D, E, Movie 10). In abnormally expanding cells, which are occasionally
312 observed in *ARKabc-1*, actin foci were barely detectable (Movie 11). We investigated
313 whether the actin phenotype could be explained within the framework of microtubule-
314 based transport driven by ARK. In animals, proper actin organisation and dynamics for
315 cell motility require the activation of Rho family small GTPases (called ROP in plants),
316 which then activate the actin polymerisation factors formin and the Arp2/3 complex [56–
317 58]. The cortical localisation of function-verified Rop4-mNG [59] was unchanged in the
318 *ARKabc-1* mutant (Fig. S5C). Interestingly, however, in *ARKabc-1* we observed a

319 reduction in the cortical signals from RopGEF3 and RopGEF6, the guanine nucleotide
320 exchange factor (GEF) of ROP, and For2A (class II formin) and Arp3a, which are
321 required for rapid actin elongation and formation of actin filaments during cell tip growth
322 in moss [60,61] (Fig. 6A–F, Fig. S5D, Movies 12–14). This was unlikely due to reduced
323 protein expression levels in the *ARKabc-1* mutant, as RopGEF and For2A protein levels
324 did not decrease substantially according to immunoblotting results (Fig. S7). Consistent
325 with these signal reductions, oblique illumination microscopy revealed that the growth
326 rate of actin filament near the tip was reduced by 14% compared to that in the control line
327 (Fig. 5F, Movie 15). Furthermore, similar to F-actin, the loss of apical enrichment of
328 RopGEF and For2A signals was temporally correlated with cell swelling (Movies 16–
329 18). Other RopGEFs tagged with mNG were either undetectable or very weakly
330 expressed; therefore, they were not studied further. The necessity of microtubules for
331 apical enrichment of RopGEF3 and RopGEF6 was confirmed by oryzalin treatment
332 followed by time-lapse microscopy (Fig. S5E, F).
333 We reasoned that if the tip growth defect in the *ARK* mutant could be attributed to a
334 defect in the apical transport of actin regulatory molecules, the ectopic expression and
335 forced apical localisation of RopGEFs would restore the tip growth of the *ARKabc-1*
336 mutant. To test this hypothesis, we ectopically expressed RopGEF3-mNG in *ARKabc-1*.
337 Plant growth slightly recovered in the transgenic line (Fig. 6H, J). Next, we constructed
338 a fusion gene in which tail-deleted ARKb was fused to RopGEF3-mNG and expressed it
339 in *ARKabc-1* (Fig. 6G). As expected from a protein with the plus-end-directed motility,
340 the fusion protein was enriched at the apical cell tip (Fig. 6H, bottom). However, because
341 the ARM domain was absent in this construct, the chloroplast distribution was not
342 restored (Fig. 6I). However, the fusion construct substantially restored protonemal growth
343 (Fig. 6H, J). Thus, the forced delivery of RopGEF3 to the cell tip using an anterograde
344 motor was sufficient to restore cell tip growth.
345
346 **Partial complementation of Pp*ARK* mutant by AtARK2 and AtARK3**
347 Finally, we examined whether ectopic expression of *A. thaliana* ARK could rescue
348 the moss *ARK* mutant phenotypes. To this end, we attempted to express AtARK1,
349 AtARK2, and AtARK3 in moss *ARKabc-1*. For unknown reasons, transformants
350 expressing AtARK1 could not be obtained, despite multiple attempts. In contrast, lines
351 stably expressing AtARK2-mNG or AtARK3-mNG were successfully generated. The
352 moss expressing AtARK2 or AtARK3 grew slightly faster than the parental *ARKabc-1*
353 line, and the protonemal tissue was observed more clearly on the culture plate (Fig. 7A,
354 top). Robust growth of the protonemal filament was also observed in the images of a 6-
355 day-old protonema regenerated from a single protoplast (Fig. 7A, bottom). Rhizoid
356 growth was also promoted (Fig. S8A-B). Thus, AtARK2 and AtARK3 partially rescued
357 the growth phenotype. In contrast, AtARK did not rescue the nuclear position (Fig. 7B,
358 arrowheads). The basal accumulation of chloroplasts in *ARKabc-1* disappeared after
359 ectopic expression of AtARK2 but not that of AtARK3 (Fig. 7B, C). Moreover, AtARK2
360 expression resulted in an apical shift of the chloroplast, which is somewhat reminiscent
361 of the *KCBP* knockout line [25]. Ectopic AtARK2 or AtARK3 expression did not affect the
362 microtubule dynamics (Fig. S8C). We conclude that AtARK2 and AtARK3 can substitute
363 for a subset of moss ARK functions.
364

365 # Discussion
366
367 **ARK is a versatile anterograde transporter in *P. patens***
368 An anterograde transporter that can carry various cargos is a long sought-after in
369 plant microtubule biology [3,62–64], although microtubule-dependent transport has been
370 reported in multiple cell types [18–22]. Several data presented in this study suggest that it
371 could be ARK, which is a widely conserved kinesin in plants.
372 First, the movement of three giant organelles and RabA2-marked vesicles was
373 suppressed in the *ARKabc* triple mutant. Because movement towards the apex was
374 suppressed and microtubule polarity was unchanged in the mutant, we concluded that
375 ARK is responsible for the plus-end-directed motility of these organelles. Using
376 *ARKabcd-1*, we also demonstrated that microtubule polymerisation dynamics were
377 unperturbed in the absence of ARK. Thus, an alternative microtubule-based mechanism,
378 namely, microtubule polymerisation-based pushing [34,65], is unlikely to be the cause of
379 abnormal motility. The most natural interpretation is that ARK transports cargo to the
380 microtubule plus-end. We speculate that the residual apical motility observed in the
381 *ARKabc-1* mutant is driven by the intact ARKd protein. However, the possibility that
382 additional motor families also play a role in the transport of these cargo cannot be ruled
383 out. For example, in Arabidopsis, vesicular transport on cortical microtubules requires
384 the FRA1 protein, which is a processive, plus-end-directed kinesin belonging to the
385 kinesin-4 family [66–68].
386 Second, we detected the processive motility of ARKb proteins *in vivo* and *in vitro*.
387 A single ARK motor can run on microtubules unidirectionally for over a micron,
388 suggesting that ARK can serve as long-distance transporters. In contrast to wild-type
389 ARKb, the rigor mutant did not show motility or rescue the mutant phenotype, consistent
390 with the notion that ARKb acts as a transporter rather than as an activator of an unknown
391 transporter. However, it remains unclear whether the motile ARKb-mNG signals *in vivo*
392 represent cargo-carrying or cargo-free ARKb proteins. Because a significant population
393 of ARK proteins are bound to microtubules but are not motile, an intriguing possibility is
394 that cargo binding activates the motor and initiates motility.
395 Finally, ARK localises to the nuclear surface in a tail region-dependent manner, and
396 the tail is critical for nuclear and chloroplast motility. The tail region is essential for the
397 function of cargo-carrying kinesins, because it is generally the binding site for cargo. In
398 contrast, the tail of kinesin-13 or AtARK1 is dispensable for the regulation of microtubule
399 dynamics [51,69]. A dominant-negative effect of the tail is also consistent with the model in
400 that it serves as the cargo-binding site.
401 Taken together, ARK is the strongest candidate for a versatile anterograde transporter
402 in moss, which carries a variety of cargos, including nuclei, chloroplasts, mitochondria,
403 and vesicles, towards the microtubule plus ends (Fig. 7D).
404
405 **Microtubule-dependent transport supports tip growth**
406 Tip growth is a growth form found in several plant cell types, such as pollen tubes,
407 root hairs, and moss protonemata [70], as well as in many other systems, including
408 macroalgae, fungi, and neural axons in animals [71–73]. Regulated plasticisation of the cell
409 wall and vesicular transport of membrane and cell wall materials are important factors in
410 the tip growth of walled organisms [72,74]. Regarding the cytoskeleton, the primary player

411 in tip growth is actin. For example, in *P. patens* protonemata, the addition of actin
412 inhibitors immediately and completely stops tip growth [53]. In contrast, microtubules are
413 thought to play a role in determining growth orientation. Cell tip expansion and abnormal
414 outgrowth in non-apical regions have been reported after the addition of microtubule-
415 depolymerising drugs [53]. However, the detailed mechanism by which microtubules define
416 growth direction remains elusive.
417 Our analyses suggest that the microtubule- and ARK-dependent transport of actin
418 regulatory molecules is critical for polarised tip growth. First, the rigor mutant of ARK
419 could not restore tip growth. Second, actin regulatory molecules (RopGEF3, RopGEF6,
420 For2A, and Arp3a) and F-actin were less enriched at the apex in the *ARKabc-1* mutant
421 and restored by exogenous ARKb expression. Third, and most notably, the growth
422 phenotype was partially rescued by the artificial delivery of RopGEF3 to the apex by
423 tailless ARKb. This result suggests that in wild-type moss, RopGEF or the upstream
424 factor required for RopGEF localisation is transported by ARK. This experiment also
425 suggested that the growth defect was independent of organelle mispositioning, as the
426 fusion construct failed to rescue organelle distribution. Only a partial rescue of the growth
427 phenotype by RopGEF force-localisation suggests that ARK transports other molecules
428 critical for tip growth in addition to actin regulators. Identification of the cargo molecules
429 would further clarify the versatility of ARK as a transporter and the detailed molecular
430 mechanism of ARK-dependent tip growth.
431 Among the tip-growing cells in plants, protonemal cells in Physcomitrella are
432 characterised by the development of endoplasmic, but not cortical, microtubules [75].
433 However, conceptually, the mechanism by which ARK-dependent anterograde transport
434 regulates polarised cell growth is remarkably similar to what has been revealed in the
435 fission yeast *Schizosacharomyces pombe*, an organism with one of the best-studied cell
436 growth systems [76]. In fission yeast, bipolar cell growth during interphase is ensured by
437 bipolar microtubule networks and the plus-end and cortical accumulation of the Tea1-
438 Tea4 complex, which recruits formin For3 [77,78]. The molecule important for Tea1-Tea4
439 localisation is the processive, plus-end-directed kinesin Tea2 [79–81]. In the absence of Tea2,
440 cells that initiate growth from improper sites are observed, which is likely driven by actin
441 that is not restricted to a single site [79]. An analogous mechanism is found in the
442 filamentous fungus *Aspergillus nidulans* [72]. Interestingly, the transport of polarity factors
443 by anterograde motors is critical for cell morphogenesis also in mammalian cells. In
444 epithelial cells, microtubules form uniform arrays along the apico-basolateral polarity
445 axis, and several anterograde kinesins have been suggested to transport key polarity
446 proteins associated with epithelial morphogenesis [82–84]. Thus, long-distance transport of
447 polarisation factors along microtubules might be a general scheme for polarised growth
448 in a wide range of eukaryotic cells.
449
450 **Possible ARK function beyond moss protonemata**
451 ARK genes are conserved in land plants, but are absent in algae or animals [35].
452 However, the overall ARK structure is typical for kinesin superfamily proteins, where the
453 motor domain and coiled-coil are followed by a cargo-recognising tail. As ARM repeats
454 are commonly found in eukaryotes, including red and green algae, land plants may have
455 acquired ARK through a fusion event between kinesin motor domain and ARM.
456 The functions of ARK in land plants are likely to be diversified. Liverwort ARK was

457 shown to be required for organelle movement, including the nuclei and plastids,
458 illustrating ARK conservation as a transporter in bryophytes [35]. In contrast, AtARK1, the
459 best-studied ARK in angiosperms, regulates microtubule dynamics, and the mutant
460 phenotype appears to be well-explained by the lack of this activity [32,51]. Whether AtARK1
461 also has a transport function remains unknown. Interestingly, we observed that AtARK2
462 and AtARK3 partially restored chloroplast distribution and protonemal growth in *P.*
463 *patens ARKabc-1* mutant without altering microtubule polymerisation dynamics. Thus,
464 the cargo-carrying activity may be preserved in Arabidopsis ARK. The *AtARK2* mutant
465 showed helical root growth and longer hypocotyls, indicating that AtARK2 is required
466 for proper growth of root epidermal cells and hypocotyl cells [85,86]. AtARK3 is essential
467 for plant development [87]. Abnormal distribution of stomata was observed upon cell type-
468 and cell cycle-specific AtARK3 knockdown in stomatal meristemoid mother cells [88].
469 Whether these phenotypes are caused by mislocalisation of AtARK cargo remains to be
470 studied.
471 Our cellular analysis was conducted only in protonema, which is excellent for
472 analysing microtubule polymerisation dynamics and microtubule-based transport.
473 However, moss ARK plays an important role in rhizoids and gametophores, as their
474 development is abnormal in *ARKabcd-1*. It is currently unclear whether these defects can
475 be attributed to the loss of anterograde transport. Moss ARK might have additional
476 functions, such as microtubule convergence [35]. In addition, some phenotypes associated
477 with *ARK* mutations might be caused by the secondary effect of nuclear mispositioning
478 or unbalanced force application on the nucleus, which could skew cellular signalling and
479 gene expression [89–91]. Determining the specific intracellular defect attributable to each
480 phenotype is an interesting topic for future research.
481

482 ## Materials and methods

483

484 ### *P. patens* culture and transformation

485 All strains in this study were derived from the Gransden ecotype of *Physcomitrium*
486 (*Physcomitrella*) *patens* [92]. *P. patens* culture and transformation protocols followed were
487 as described by Yamada et al. (2016). Briefly, mosses were regularly cultured on BCDAT
488 plates at 25 °C under continuous light illumination. A standard polyethylene glycol
489 (PEG)-mediated method was exploited for transformation. Prior to transformation,
490 sonicated protonemata were cultured on BCDAT agar medium for 5–6 days. Transgenic
491 lines were selected using corresponding antibiotics. Line confirmation was conducted
492 through visual inspection followed by genotyping PCR (Fig. S9, Table S7) and.
493 Sequencing was performed to confirm the CRISPR mutant lines. The lines generated in
494 this study are listed in Table S4.
495

496 ### Plasmid construction

497 The plasmids and primers used in this study are listed in Tables S5 and S6, respectively.
498 CRISPR targets with high specificity were manually selected around the ATPase motif
499 (P-loop) or microtubule binding site (called the Switch 2 region) in the motor domain of
500 *ARK* genes. All target sequences were synthesised and ligated into the *Bsa*I site of
501 pPY156, which is based on pCasGuide/pUC18 and contains a hygromycin-resistant

502 cassette [93]. For endogenous tagging via homologous recombination, the plasmid was
503 constructed using the In-Fusion HD Cloning Kit (Takara); 1–2 kb sequences of the 5′ and
504 3′ ends of the genes of interest flanked the fragment that consisted of an in-frame linker,
505 mNeonGreen (mNG) coding sequence, Flag tag, and G418 resistant cassette. The mNG
506 codon was optimised for expression in Arabidopsis [38]. To generate the Rop4-mNG
507 plasmid, the fusion constructs were constructed as described by Cheng et al. (2020). For
508 all the rescue experiment, the *ARKb* coding sequence was amplified from the moss cDNA
509 library (full-length, truncation, mutant) and ligated into the pENTR/D-TOPO vector
510 containing the in-frame linker, mNG-coding sequence, and Flag tag, followed by the
511 Gateway LR reaction (Invitrogen) into the pPY138 vector containing the *P. patens EF1α*
512 promoter, G418 resistance cassette, and 1-kb sequences homologous to the *hb7* locus.
513 Likewise, the gene sequences of *A. thaliana ARK2* and *ARK3* were amplified from a
514 cDNA library (a gift from Dr. Hidefumi Shinohara [Fukui Prefectural University]) and
515 cloned into an overexpression vector containing the *EF1α* promoter.
516
517 **Moss growth assay**
518 To prepare the protoplasts, 5–7-day-old sonicated protonemata were digested with an 8%
519 (w/v) mannitol solution supplemented with 1% (w/v) driselase for 0.5–1 h. After
520 removing the driselase by washing twice with 8% mannitol solution, the protoplasts were
521 resuspended in the protoplast regeneration liquid [54,94]. After 4 h of incubation in the dark,
522 the protoplasts were collected by centrifugation, resuspended in 7.5 mL of protoplast
523 regeneration media (PRM) solution [94], and spread onto three PRM plates covered with
524 cellophane. The protoplasts were cultured for 3 days and transferred to a BCDAT plate.
525 Images of 7-day-old moss protonemata were taken using a stereomicroscope SMZ800N
526 (Nikon) equipped with an ILCE-QX1 camera (SONY). Nine-day-old protonemata were
527 inoculated onto BCDAT plates and cultured for 3–5 weeks. Images of overall moss or
528 gametophores were captured using a C-765 Ultra Zoom digital camera (Olympus) or
529 SMZ800N, respectively.
530
531 **Protein purification**
532 Protein purification was conducted as described Leong et al. (2020) with slight
533 modifications. The motor domain of ARKb (1–613 aa) was fused to sfGFP and 6×His at
534 the C-terminus. ARKb-sfGFP expression was induced in *E. coli* SoluBL21 strain with
535 0.2 mM isopropyl β-D- thiogalactopyranoside (IPTG) for 21 h at 18 °C. The cultured
536 cells were lysed in lysis buffer (25 mM MOPS pH 7.0, 250 mM KCl, 2 mM $MgCl_2$, 1
537 mM EGTA, 20 mM imidazole, and 0.1 mM ATP) supplemented with 5 mM β-
538 mercaptoethanol and protease inhibitors [1 mM phenylmethylsulfonyl fluoride (PMSF)
539 and peptide inhibitor cocktail [1 μg/mL aprotinin, 1 μg/mL chymostatin, 1 μg/mL
540 leupeptin, and 1 μg/mL pepstatin A]). After rotation with nickel-nitrilotriacetic acid (Ni-
541 NTA) beads for 1 h at 4 °C, the proteins were eluted using 500 μL elution buffer (25 mM
542 MOPS pH 7.0, 250 mM KCl, 2 mM MgCl2, 1 mM EGTA, 200 mM imidazole, and 0.1
543 mM ATP). The elution was repeated eight times. The purified proteins were flash frozen
544 and stored at -80 °C after supplementation with 40% sucrose.
545
546 ***In vitro* single kinesin motility assay**

547 The single kinesin motility assay was conducted as described Naito and Goshima (2015)
548 with slight modifications. The silanised coverslip was washed with 1× SAB (250 mM
549 MOPS pH 7.0, 750 mM KCl, 20 mM $MgCl_2$, 10 mM EGTA) and coated with anti-biotin
550 (5% in 1× SAB; Invitrogen), and the nonspecific surface was blocked with Pluronic F127
551 (1% in 1× MRB80; Invitrogen). Biotinylated microtubule seeds (50–100 μM tubulin mix
552 containing 10% biotinylated pig tubulin and 10% Alexa Fluor 647–labelled pig tubulin
553 with 1 mM GMPCPP) were specifically attached to the functionalized surface using
554 biotinylated tubulin–anti-biotin links. After the chamber was washed with 1× SAB, 500
555 pM–1 nM ARKb-sfGFP in the assay buffer (1× SAB, 75 mM KCl, 1 mM ATP, 0.5 μg/μL
556 κ-casein, and 0.1% methylcellulose) and an oxygen scavenger system (50 mM glucose,
557 400 μg/mL glucose oxidase, 200 μg/mL catalase, and 4 mM DTT) were added to the
558 chamber. The samples were sealed with candle wax. During experiments, the samples
559 were maintained at approximately 25 °C. Prior to the time-lapse imaging of GFP, a
560 microtubule image was captured. GFP images were acquired every 200–400 ms for 1 min
561 using a total internal reflection fluorescence (TIRF) microscope.
562

563 **Immunoprecipitation and western blotting**

564 Immunoprecipitation and western blotting were conducted as previously described Yi and
565 Goshima (2020) with slight modifications. Sonicated protonemata were ground in liquid
566 nitrogen and resuspended in incubation buffer (25 mM HEPES-KOH pH 7.6, 50 mM
567 NaCl, 500 μM $MgCl_2$, 500 μM EGTA, 1 mM DTT, 1% NP-40, 1× protease inhibitor
568 cocktail, and 1 mM PMSF) for immunoprecipitation. The supernatant of centrifuged
569 lysate was incubated with 20 μL anti-DDDDK-tag pAb Agarose beads (Rabbit,
570 Polyclonal, MBL) at 4 °C for 2–3 h. The beads were washed three times with wash buffer
571 (25 mM HEPES-KOH pH 7.6, 50 mM NaCl, 500 μM $MgCl_2$, 500 μM EGTA, 1× protease
572 inhibitor cocktail, and 1 mM PMSF) and boiled in a 30 μL SDS-PAGE sample buffer
573 supplemented with 1.8 M urea. Boiled samples were subjected to SDS-PAGE using 5–
574 20% premade acrylamide gel (ATTO), followed by immunoblotting using primary anti-
575 mNeonGreen antibody (mouse, monoclonal, 1:1000, Chromo Tek) and a horseradish
576 peroxidase-conjugated anti-mouse secondary antibody (1:4000). The protein signals were
577 detected using enhanced chemiluminescence (ECL) detection reagents (Cytiva).
578

579 **Microscopy**

580 Time-lapse microscopy was performed as described by Nakaoka et al. (2012). Briefly, in
581 the long-term time-lapse imaging experiments for the observation of protonemal cells,
582 the protonemata were cultured on thin layers of BCD agarose in 6-well glass-bottom
583 dishes for 5–7 days. Wide-field, epifluorescence images were acquired with a Nikon Ti
584 microscope (10× 0.45 NA lens, Zyla 4.2P CMOS camera (Andor), Nikon Intensilight
585 Epi-fluorescence Illuminator) at intervals of 3–30 min with white light between
586 acquisitions. For high-resolution imaging, protonemata were inoculated onto the agar pad
587 in a 35 mm glass-bottom dish, followed by culturing for 5–7 days. Confocal imaging was
588 performed with a Nikon Ti microscope attached to a CSU-X1 spinning-disc confocal
589 scanner unit (Yokogawa), EMCCD camera (ImagEM, Hamamatsu), and three laser lines
590 (637, 561, and 488 nm). Lenses were selected depending on the experiment (40× 1.30
591 NA, 60× 1.40 NA, and 100× 1.45 NA). Oblique illumination fluorescence microscopy

592 was performed using a Nikon Ti microscope attached to a total internal reflection
593 fluorescence (TIRF) unit, 100× 1.49-NA lens, GEMINI split view (Hamamatsu), and
594 EMCCD camera Evolve (Roper) [46]. The samples for oblique imaging were prepared with
595 a microfluidic device of 15 μm height. Stock solutions of oryzalin, latrunculin A, and
596 FM4-64 in DMSO were diluted with distilled water to working concentrations of 10 μM
597 oryzalin, 25 μM latrunculin A, and 10 μM FM4-64. Prior to drug addition, the protonemal
598 tissue on the agarose pad was preincubated in water for 1 h for absorption. After water
599 removal, 1 mL of the drug solution was added, and image acquisition was started
600 immediately. DMSO was used as a control. To induce RNAi, 1 μM β-estradiol was added
601 to the 4–5-day-old protonemata on sample dishes 12 h prior to observation. Most of the
602 imaging was performed at 22–25 °C in the dark, except for the images shown in Figure
603 S6A, which were taken under continuous light.
604
605 **Image data analysis**
606 All raw data processing and measurements were performed using the Fiji software.
607
608 *Moss growth on the culture plate.* The images of the moss on the culture plate were
609 outlined automatically, and the area was measured using Fiji.
610
611 *Rhizoid length.* Gametophore images were obtained using a stereoscopic microscope, and
612 the rhizoid length was manually measured using Fiji.
613
614 *Velocity and run length of ARKb* (*in vivo* and *in vitro*). Oblique illumination time-lapse
615 images (*in vivo*) of the endoplasmic microtubules in protonemal cells or TIRF time-lapse
616 images (*in vitro*) were taken every 200–400 ms using a 100× 1.49-NA lens. The
617 microtubules on which single or multiple fluorescent ARKb particles were continuously
618 moving were manually selected and analysed. A kymograph was generated along the
619 microtubule, and the inclination and distance of the line derived from ARKb particles
620 were measured as the velocity and run length, respectively.
621
622 *Microtubule plus-end dynamics and orientation.* To quantify the plus end
623 growth/shrinkage rate and rescue/catastrophe frequency, we followed the protocol
624 described by Leong et al. (2020). Briefly, oblique illumination time-lapse images of
625 endoplasmic microtubules in protonemal cells were taken every 3 s for 3 min using a
626 100× 1.49-NA lens. Then, a 5×6 μm² area was randomly selected in each cell, and
627 kymographs of every traceable microtubule plus end in the area were created. The
628 inclination of the microtubules in the kymographs, which corresponded to the growth or
629 shrinkage rate, was measured. To determine catastrophe or rescue frequency, the number
630 of events was counted and divided by the observed growth or shrinkage duration of the
631 microtubule, respectively. The growth rate at the cell apex was specifically determined
632 using EB1-Citrine imaging, which tracks growing plus ends. Time-lapse images of EB1-
633 Citrine were acquired every 3 s using a spinning-disc confocal microscope. Kymographs
634 were generated along the edge of the caulonemal cell apex. The inclination of EB1-Citrine
635 signals was measured to determine the microtubule growth rate. To analyse microtubule

636 orientation in interphase apical cells, cells were observed for > 150 min after anaphase
637 onset. Kymographs were generated along the edges of the cells, and the directionality of
638 EB1-Citrine comets was measured to determine the overall orientation of the
639 microtubules [96].
640
641 *Actin growth rate.* Images of apical cell tips of the Lifeact-mNG expressing line were
642 taken every 200 ms using TIRF microscopy and a 100× 1.49-NA lens. The elongating
643 Lifeact-mNG at the cell tip was tracked and used to generate kymographs. The inclination
644 of the Lifeact-mNG on the kymograph was measured as the growth rate of the actin
645 filament. We noted that actin dynamics parameters were sensitive to the expression levels
646 of Lifeact-mNG. Therefore, we used the same parental line expressing Lifeact-mNG in
647 this experiment and analysis.
648
649 *Spindle position and cell length.* For caulonemal apical cells, time-lapse images were
650 obtained every 3 min using an epifluorescence (wide-field) microscope and a 10× 0.45
651 NA lens, and the distance between the basal cell wall and cell tip (i.e. cell length) or the
652 spindle equator was measured just before anaphase onset. The relative position of the
653 metaphase spindle was determined using division.
654
655 *Subapical cell length*. Images of moss protonemata stained with FM4-64 were obtained
656 using an epifluorescence (wide-field) microscope with z-stacks at 5 µm intervals for a
657 range of 150 µm. using a 10× 0.45 NA lens. The lengths of the subapical cells of the
658 caulonemal filaments were measured (single z plane).
659
660 *Cell cycle duration*. Time-lapse images of the caulonemal cells were obtained every 10
661 min using an epifluorescence (wide-field) microscope and a 10× 0.45 NA lens. The
662 duration between the nuclear envelope breakdown (NEBD) of the mother cell and the
663 NEBD of the daughter apical cell was measured.
664
665 *Nuclear movement.* Time-lapse images were taken every 3 min using a spinning-disc
666 confocal microscope and a 40× 1.30 NA lens with z-stacks at 2.5–5 µm intervals for a
667 range of 5–10 µm. The distance between the cell plate and centre of the nucleus was
668 measured in apical cells before and after cell division.
669
670 *Chloroplast distribution.* Time-lapse images were taken every 3 min using an
671 epifluorescence (wide-field) microscope and a 10× 0.45 NA lens. The intensity of
672 chloroplast autofluorescence along the long axis of caulonemal apical cells was measured
673 150 min after anaphase onset, and the background intensity of each image was subtracted.
674 The intensity of each pixel on the drawn line was divided by the mean intensity of the
675 entire length of the line to get relative intensity. The cells were divided into ten sections,
676 and the average relative intensity of each section is displayed.
677

678 *Mitochondrial movement.* To visualise mitochondria, γ-F1ATPase-mNG was expressed
679 under the *EF1α* promotor [97]. Movies and kymographs were created from images acquired
680 every 2 s using oblique illumination fluorescence microscopy. To quantify mitochondrial
681 relocation, time-lapse images of the apical side of caulonemal apical cells were obtained
682 every 10 s for 6 min using spinning-disc confocal microscopy and a 100× 1.45 NA lens.
683 The majority of the microtubules in this area are oriented in such a manner that the plus
684 ends face the apex [23], enabling a reliable estimate of whether mitochondria tend to move
685 towards the plus or minus end. In this analysis, 15 μm^2 was selected in the area between
686 the cell apex and nucleus, and 12 mitochondria that were clearly identified were analysed.
687 The position of each mitochondrion in the first and last frame was compared; based on
688 the overall microtubule polarity, translocation towards the tip was interpreted as
689 anterograde motility.
690
691 *Intensity of mNG-RabA2b, For2A-mNG, and Arp3a-mNG.* The apex of caulonemal cells
692 in which mNG-RabA2b, For2A-mNG, or *Arp3a-mNG* was expressed was imaged using
693 a z-series taken every 0.5 µm for a range of 15 µm using a spinning-disc confocal
694 microscope and a 100× 1.45 NA lens. The mean intensity within approximately 2 μm^2 of
695 the punctate signals was measured and subtracted by the cytoplasmic background
696 intensity.
697
698 *Movement of mNG-RabA2b puncta.* Images of caulonemal apical cells expressing mNG-
699 RabA2b were taken every 200 ms using a spinning-disc confocal microscope and a 100×
700 1.45 NA lens. The number of signal puncta moving >10 µm in a minute was counted for
701 each cell.
702
703 *Nuclear motility rate.* Time-lapse epifluorescence (wide-field) images of protonemata
704 were obtained every 3 min using a 10× 0.45 NA lens. The apical motility of the nucleus
705 after cell division was manually measured using the Fiji software.
706
707 *Chloroplast motility rate*. Chloroplasts in interphase caulonemal apical cells were imaged
708 every 3 s using a spinning-disc confocal microscope and a 60× 1.40 NA lens. The apical
709 motility of chloroplasts was manually measured using Fiji.
710
711 *Mitochondrial motility rate.* Mitochondria in interphase caulonemal apical cells were
712 imaged every 1.5 s using a spinning-disc confocal microscope and a 100× 1.45 NA lens.
713 The apical motility of mitochondria was manually measured using Fiji.
714
715 *Motility rate of RabA2b-positive vesicle.* Vesicles in interphase caulonemal apical cells
716 were imaged every 200 ms using a spinning-disc confocal microscope and a 100× 1.45
717 NA lens. The apical motility of the vesicle was manually measured using Fiji.
718
719 *Tip growth rate.* Time-lapse epifluorescence (wide-field) images of protonemata were
720 obtained every 3 min using a 10× 0.45 NA lens. Kymographs were created along the axes

721 of growing caulonemal filaments, and the slope of the kymographs was measured to
722 obtain the growth rate.
723
724 *Cell morphology observation under ARKd RNAi*. The moss protonemata were cultured
725 on BCDAT for 4–5 days, and 1 μM β-estradiol or the control (0.1% DMSO) was added
726 to the plant. After four days of incubation following drug addition, the morphology of the
727 apical cells was observed and counted. Time-lapse images were obtained using a wide-
728 field microscope under constant transmission light (20× 0.75 NA lens).
729
730 *Frequency of actin foci formation at the cell apex.* The apexes of the cells expressing
731 Lifeact-mNG was imaged using a z-series taken every 0.5 μm for a range of 4 μm for 5
732 min at 5 s intervals with a spinning-disc confocal microscope and a 100× 1.45 NA lens.
733 The z-stack images were processed by maximum z-projection with Fiji, and the number
734 of time frames in which the actin focus was clearly observed was counted. The ratio of
735 time frames with clear foci was used to determine the frequency of foci formation.
736
737 *Intensity of Rop4-mNG and RopGEFs-mNG.* The protonemal cell apex of the cell line
738 expressing Rop4-mNG or RopGEFs-mNG was imaged using a z-series taken every 0.5
739 μm for a range of 15 μm with a spinning-disc confocal microscope and a 100× 1.45 NA
740 lens. A slice showing the centre of the cell was selected. The total intensity of mNG
741 signals was measured along the cell edge by drawing a line (width = 0.4 μm) (subtracted
742 by the cytoplasmic background intensity). ROP-GEF6 was distributed more broadly than
743 ROP-GEF3. For the analysis of the temporal change of the intensity under the drug
744 treatment, time-lapse images were acquired every 1 or 3 min using a z-series taken every
745 1.5 μm for a range of 6 μm. The images were quantified in an identical manner.
746
747 **Statistical analysis**
748 The Shapiro-Wilk test was used for all samples to check for normality. If the sample was
749 assumed to be normally distributed, the F-test (two groups) or Bartlett's test (multiple
750 groups) was conducted to test homoscedasticity. If the samples had a normal distribution
751 and equal variance, Student's *t*-test (two groups) or Tukey's multiple comparison test
752 (multiple groups) was used. If the samples had a normal distribution but not equal
753 variance, Welch's two-sample *t*-test (two groups) or the Games-Howell test (multiple
754 groups) was used. If the samples did not have a normal distribution, Mann-Whitney U test
755 (two groups) or Steel-Dwass test (multiple groups) was used. All statistical analyses were
756 performed using R software. Obtained P values are denoted as follows: *, $P < 0.05$; **, P
757 < 0.01; ***, $P < 0.001$; and ****, $P < 0.0001$. Data from multiple experiments were
758 combined because of insufficient sample numbers in a single experiment unless otherwise
759 stated.
760
761 **Accession numbers**
762 The gene sequences used in this study are available in Phytozome under the following
763 accession numbers: *AtARK1* (AT3G54870.3), *AtARK2* (AT1G01950.3), *AtARK3*
764 (AT1G12430.1), *PpARKa* (Pp3c27_850V3.1), *PpARKb* (Pp3c16_2830V3.1), *PpARKc*

(Pp3c6_19520V3.1), *PpARKd* (Pp3c2_28162V3.1). More information is available in Table S5.

Acknowledgements

We are grateful to Magdalena Bezanilla, Peishan Yi, and Moé Yamada for providing the moss lines and plasmids; Noiri Oguri, Chiemi Koketsu and Rie Inaba for media preparation; and Hiroyasu Motose for communicating unpublished data. This work was funded by the Japan Society for the Promotion of Science KAKENHI (17H06471, 18KK0202, 22H04717, and 22H02644 to GG). MWY is a recipient of the Japan Society for the Promotion of Science pre-doctoral fellowship. The authors declare that they have no conflicts of interest.

References

1. Hirokawa, N. & Noda, Y. Intracellular Transport and Kinesin Superfamily Proteins, KIFs: Structure, Function, and Dynamics. *Physiological Reviews* **88**, 1089–1118 (2008).
2. Reck-Peterson, S. L., Redwine, W. B., Vale, R. D. & Carter, A. P. The cytoplasmic dynein transport machinery and its many cargoes. *Nat Rev Mol Cell Biol* **19**, 382–398 (2018).
3. Vale, R. D. The Molecular Motor Toolbox for Intracellular Transport. *Cell* **112**, 467–480 (2003).
4. Encalada, S. E. & Goldstein, L. S. B. Biophysical Challenges to Axonal Transport: Motor-Cargo Deficiencies and Neurodegeneration. *Annual Review of Biophysics* **43**, 141–169 (2014).
5. Hirokawa, N., Niwa, S. & Tanaka, Y. Molecular Motors in Neurons: Transport Mechanisms and Roles in Brain Function, Development, and Disease. *Neuron* **68**, 610–638 (2010).
6. Vale, R. D., Reese, T. S. & Sheetz, M. P. Identification of a novel force-generating protein, kinesin, involved in microtubule-based motility. *Cell* **42**, 39–50 (1985).
7. Leopold, P. L., McDowall, A. W., Pfister, K. K., Bloom, G. S. & Brady, S. T. Association of kinesin with characterized membrane-bounded organelles. *Cell Motility* **23**, 19–33 (1992).
8. Nakata, T. & Hirokawa, N. Microtubules provide directional cues for polarized axonal transport through interaction with kinesin motor head. *The Journal of cell biology* **162**, 1045–1055 (2003).
9. Splinter, D. *et al.* Bicaudal D2, Dynein, and Kinesin-1 Associate with Nuclear Pore Complexes and Regulate Centrosome and Nuclear Positioning during Mitotic Entry. *PLOS Biology* **8**, e1000350 (2010).
10. Tanaka, Y. *et al.* Targeted Disruption of Mouse Conventional Kinesin Heavy Chain kif5B, Results in Abnormal Perinuclear Clustering of Mitochondria. *Cell* **93**, 1147–1158 (1998).
11. Zimyanin, V. L. *et al.* In Vivo Imaging of oskar mRNA Transport Reveals the Mechanism of Posterior Localization. *Cell* **134**, 843–853 (2008).
12. Rogers, S. L. & Gelfand, V. I. Membrane trafficking, organelle transport, and

811 the cytoskeleton. *Current Opinion in Cell Biology* **12**, 57–62 (2000).
812 13. Welte, M. A. Bidirectional Transport along Microtubules. *Current Biology* **14**,
813 R525–R537 (2004).
814 14. Shimmen, T. & Yokota, E. Cytoplasmic streaming in plants. *Current Opinion*
815 *in Cell Biology* **16**, 68–72 (2004).
816 15. Tominaga, M. & Ito, K. The molecular mechanism and physiological role of
817 cytoplasmic streaming. *Current Opinion in Plant Biology* **27**, 104–110 (2015).
818 16. Tamura, K. *et al.* Myosin XI-i Links the Nuclear Membrane to the
819 Cytoskeleton to Control Nuclear Movement and Shape in Arabidopsis. *Current Biology*
820 **23**, 1776–1781 (2013).
821 17. Kong, S.-G. & Wada, M. Molecular basis of chloroplast photorelocation
822 movement. *Journal of plant research* **129**, 159–166 (2016).
823 18. Frey, N., Klotz, J. & Nick, P. A kinesin with calponin-homology domain is
824 involved in premitotic nuclear migration. *Journal of Experimental Botany* **61**, 3423–
825 3437 (2010).
826 19. Katsuta, J. & Shibaoka, H. The roles of the cytoskeleton and the cell wall in
827 nuclear positioning in tobacco BY-2 cells. *Plant and cell physiology* **29**, 403–413
828 (1988).
829 20. Katsuta, J., Hashiguchi, Y. & Shibaoka, H. The role of the cytoskeleton in
830 positioning of the nucleus in premitotic tobacco BY-2 cells. *Journal of cell science* **95**,
831 413–422 (1990).
832 21. Muroyama, A., Gong, Y. & Bergmann, D. C. Opposing, Polarity-Driven
833 Nuclear Migrations Underpin Asymmetric Divisions to Pattern Arabidopsis Stomata.
834 *Current Biology* **30**, 4467-4475.e4 (2020).
835 22. Zonia, L., Tupý, J. & Staiger, C. J. Unique actin and microtubule arrays co-
836 ordinate the differentiation of microspores to mature pollen in Nicotiana tabacum.
837 *Journal of Experimental Botany* **50**, 581–594 (1999).
838 23. Hiwatashi, Y., Sato, Y. & Doonan, J. H. Kinesins Have a Dual Function in
839 Organizing Microtubules during Both Tip Growth and Cytokinesis in Physcomitrella
840 patens. *The Plant Cell* **26**, 1256–1266 (2014).
841 24. Yamada, M. & Goshima, G. The KCH Kinesin Drives Nuclear Transport and
842 Cytoskeletal Coalescence to Promote Tip Cell Growth in Physcomitrella patens. *The*
843 *Plant Cell* **30**, 1496–1510 (2018).
844 25. Yamada, M., Tanaka-Takiguchi, Y., Hayashi, M., Nishina, M. & Goshima, G.
845 Multiple kinesin-14 family members drive microtubule minus end–directed transport in
846 plant cells. *Journal of Cell Biology* **216**, 1705–1714 (2017).
847 26. Yoshida, M. W., Yamada, M. & Goshima, G. Moss Kinesin-14 KCBP
848 Accelerates Chromatid Motility in Anaphase. *Cell Structure and Function* **44**, 95–104
849 (2019).
850 27. Shen, Z., Collatos, A. R., Bibeau, J. P., Furt, F. & Vidali, L. Phylogenetic
851 Analysis of the Kinesin Superfamily from Physcomitrella. *Front. Plant Sci.* **3**, (2012).
852 28. Gabrych, D. R., Lau, V. Z., Niwa, S. & Silverman, M. A. Going Too Far Is the
853 Same as Falling Short†: Kinesin-3 Family Members in Hereditary Spastic Paraplegia.
854 *Frontiers in Cellular Neuroscience* **13**, (2019).
855 29. Siddiqui, N. & Straube, A. Intracellular cargo transport by kinesin-3 motors.
856 *Biochemistry Moscow* **82**, 803–815 (2017).
857 30. Miki, T., Nishina, M. & Goshima, G. RNAi Screening Identifies the Armadillo

858 Repeat-Containing Kinesins Responsible for Microtubule-Dependent Nuclear
859 Positioning in Physcomitrella patens. *Plant and Cell Physiology* **56**, 737–749 (2015).
860 31. Jonsson, E., Yamada, M., Vale, R. D. & Goshima, G. Clustering of a kinesin-
861 14 motor enables processive retrograde microtubule-based transport in plants. *Nature*
862 *Plants* **1**, 1–7 (2015).
863 32. Eng, R. C. & Wasteneys, G. O. The microtubule plus-end tracking protein
864 ARMADILLO-REPEAT KINESIN1 promotes microtubule catastrophe in Arabidopsis.
865 *Plant Cell* **26**, 3372–3386 (2014).
866 33. Sun, J., Zhang, M., Qi, X., Doyle, C. & Zheng, H. Armadillo-repeat kinesin1
867 interacts with Arabidopsis atlastin RHD3 to move ER with plus-end of microtubules.
868 *Nat Commun* **11**, 5510 (2020).
869 34. Tran, P. T., Marsh, L., Doye, V., Inoué, S. & Chang, F. A Mechanism for
870 Nuclear Positioning in Fission Yeast Based on Microtubule Pushing. *Journal of Cell*
871 *Biology* **153**, 397–412 (2001).
872 35. Kanda, A., Otani, K., Takahashi, T. & Motose, H. Plant specific armadillo
873 repeat kinesin directs organelle transport and microtubule convergence to promote tip
874 growth. 2022.07.08.499237 Preprint at https://doi.org/10.1101/2022.07.08.499237
875 (2022). (*bioRxiv*)
876 36. Miki, T., Naito, H., Nishina, M. & Goshima, G. Endogenous localizome
877 identifies 43 mitotic kinesins in a plant cell. *PNAS* **111**, E1053–E1061 (2014).
878 37. Lopez-Obando, M. *et al.* Simple and efficient targeting of multiple genes
879 through CRISPR-Cas9 in Physcomitrella patens. *G3: Genes, Genomes, Genetics* **6**,
880 3647–3653 (2016).
881 38. Yi, P. & Goshima, G. Transient cotransformation of CRISPR/Cas9 and
882 oligonucleotide templates enables efficient editing of target loci in Physcomitrella
883 patens. *Plant Biotechnology Journal* **18**, 599–601 (2020).
884 39. Kull, F. J., Sablin, E. P., Lau, R., Fletterick, R. J. & Vale, R. D. Crystal
885 structure of the kinesin motor domain reveals a structural similarity to myosin. *Nature*
886 **380**, 550–555 (1996).
887 40. Nakata, T. & Hirokawa, N. Point mutation of adenosine triphosphate-binding
888 motif generated rigor kinesin that selectively blocks anterograde lysosome membrane
889 transport. *Journal of Cell Biology* **131**, 1039–1053 (1995).
890 41. Furt, F., Lemoi, K., Tüzel, E. & Vidali, L. Quantitative analysis of organelle
891 distribution and dynamics in Physcomitrella patens protonemal cells. *BMC Plant*
892 *Biology* **12**, 70 (2012).
893 42. Orr, R. G., Cheng, X., Vidali, L. & Bezanilla, M. Orchestrating cell
894 morphology from the inside out – using polarized cell expansion in plants as a model.
895 *Current Opinion in Cell Biology* **62**, 46–53 (2020).
896 43. Chow, C.-M., Neto, H., Foucart, C. & Moore, I. Rab-A2 and Rab-A3 GTPases
897 define a trans-golgi endosomal membrane domain in Arabidopsis that contributes
898 substantially to the cell plate. *Plant Cell* **20**, 101–123 (2008).
899 44. Pang, L. *et al.* The small GTPase RABA2a recruits SNARE proteins to
900 regulate the secretory pathway in parallel with the exocyst complex in Arabidopsis.
901 *Molecular Plant* **15**, (2021).
902 45. Leong, S. Y., Edzuka, T., Goshima, G. & Yamada, M. Kinesin-13 and Kinesin-
903 8 Function during Cell Growth and Division in the Moss Physcomitrella patens. *The*
904 *Plant Cell* **32**, 683–702 (2020).

905 46. Nakaoka, Y., Kimura, A., Tani, T. & Goshima, G. Cytoplasmic nucleation and
906 atypical branching nucleation generate endoplasmic microtubules in Physcomitrella
907 patens. *The Plant Cell* **27**, 228–242 (2015).
908 47. Shaner, N. C. *et al.* A bright monomeric green fluorescent protein derived from
909 Branchiostoma lanceolatum. *Nat Methods* **10**, 407–409 (2013).
910 48. Allen, R. D., Metuzals, J., Tasaki, I., Brady, S. T. & Gilbert, S. P. Fast Axonal
911 Transport in Squid Giant Axon. *Science* **218**, 1127–1129 (1982).
912 49. Hunt, A. J., Gittes, F. & Howard, J. The force exerted by a single kinesin
913 molecule against a viscous load. *Biophysical Journal* **67**, 766–781 (1994).
914 50. Coates, J. C. Armadillo repeat proteins: beyond the animal kingdom. *Trends in*
915 *Cell Biology* **13**, 463–471 (2003).
916 51. Eng, R. C. *et al.* The ARM Domain of ARMADILLO-REPEAT KINESIN 1 is
917 Not Required for Microtubule Catastrophe But Can Negatively Regulate NIMA-
918 RELATED KINASE 6 in Arabidopsis thaliana. *Plant and Cell Physiology* **58**, 1350–
919 1363 (2017).
920 52. Russell, P. & Nurse, P. Negative regulation of mitosis by wee1+, a gene
921 encoding a protein kinase homolog. *Cell* **49**, 559–567 (1987).
922 53. Doonan, J. H., Cove, D. J. & Lloyd, C. W. Microtubules and microfilaments in
923 tip growth: evidence that microtubules impose polarity on protonemal growth in
924 Physcomitrella patens. *Journal of Cell Science* **89**, 533–540 (1988).
925 54. Vidali, L., Augustine, R. C., Kleinman, K. P. & Bezanilla, M. Profilin is
926 essential for tip growth in the moss Physcomitrella patens. *The Plant Cell* **19**, 3705–
927 3722 (2007).
928 55. Wu, S.-Z. & Bezanilla, M. Actin and microtubule cross talk mediates persistent
929 polarized growth. *Journal of Cell Biology* **217**, 3531–3544 (2018).
930 56. Burkart, G. M., Baskin, T. I. & Bezanilla, M. A family of ROP proteins that
931 suppresses actin dynamics, and is essential for polarized growth and cell adhesion. *J*
932 *Cell Sci* **128**, 2553–2564 (2015).
933 57. Etienne-Manneville, S. & Hall, A. Rho GTPases in cell biology. *Nature* **420**,
934 629–635 (2002).
935 58. Kost, B. Spatial control of Rho (Rac-Rop) signaling in tip-growing plant cells.
936 *Trends in Cell Biology* **18**, 119–127 (2008).
937 59. Cheng, X., Mwaura, B. W., Chang Stauffer, S. R. & Bezanilla, M. A fully
938 functional ROP fluorescent fusion protein reveals roles for this GTPase in subcellular
939 and tissue-level patterning. *Plant Cell* **32**, 3436–3451 (2020).
940 60. Finka, A. *et al.* The knock-out of ARP3a gene affects F-actin cytoskeleton
941 organization altering cellular tip growth, morphology and development in moss
942 Physcomitrella patens. *Cell Motility* **65**, 769–784 (2008).
943 61. Vidali, L. *et al.* Rapid formin-mediated actin-filament elongation is essential
944 for polarized plant cell growth. *Proceedings of the National Academy of Sciences* **106**,
945 13341–13346 (2009).
946 62. Asada, T. & Collings, D. Molecular motors in higher plants. *Trends in Plant*
947 *Science* **2**, 29–37 (1997).
948 63. Kaothien, P. *et al.* Kinase partner protein interacts with the LePRK1 and
949 LePRK2 receptor kinases and plays a role in polarized pollen tube growth. *Plant J* **42**,
950 492–503 (2005).
951 64. Reddy, A. S. N. Molecular motors and their functions in plants. in

952 *International Review of Cytology* vol. 204 97–178 (Elsevier, 2001).
953 65. Piel, M. & Tran, P. T. Cell Shape and Cell Division in Fission Yeast. *Current*
954 *Biology* **19**, R823–R827 (2009).
955 66. Kong, Z. *et al.* Kinesin-4 Functions in Vesicular Transport on Cortical
956 Microtubules and Regulates Cell Wall Mechanics during Cell Elongation in Plants.
957 *Molecular Plant* **8**, 1011–1023 (2015).
958 67. Zhu, C. & Dixit, R. Single Molecule Analysis of the Arabidopsis FRA1
959 Kinesin Shows that It Is a Functional Motor Protein with Unusually High Processivity.
960 *Molecular Plant* **4**, 879–885 (2011).
961 68. Zhu, C. *et al.* The fragile Fiber1 kinesin contributes to cortical microtubule-
962 mediated trafficking of cell wall components. *Plant Physiology* **167**, 780–792 (2015).
963 69. Maney, T., Wagenbach, M. & Wordeman, L. Molecular Dissection of the
964 Microtubule Depolymerizing Activity of Mitotic Centromere-associated Kinesin*.
965 *Journal of Biological Chemistry* **276**, 34753–34758 (2001).
966 70. Rounds, C. M. & Bezanilla, M. Growth Mechanisms in Tip-Growing Plant
967 Cells. *Annu. Rev. Plant Biol.* **64**, 243–265 (2013).
968 71. Dickson, B. J. Rho GTPases in growth cone guidance. *Current Opinion in*
969 *Neurobiology* **11**, 103–110 (2001).
970 72. Riquelme, M. Tip Growth in Filamentous Fungi: A Road Trip to the Apex.
971 *Annual Review of Microbiology* **67**, 587–609 (2013).
972 73. Shirae-Kurabayashi, M., Edzuka, T., Suzuki, M. & Goshima, G. Cell tip
973 growth underlies injury response of marine macroalgae. *PLOS ONE* **17**, e0264827
974 (2022).
975 74. Bibeau, J. P., Galotto, G., Wu, M., Tüzel, E. & Vidali, L. Quantitative cell
976 biology of tip growth in moss. *Plant Mol Biol* **107**, 227–244 (2021).
977 75. Doonan, J. H., Cove, D. J. & Lloyd, C. W. Immunofluorescence microscopy of
978 microtubules in intact cell lineages of the moss, Physcomitrella patens. I. Normal and
979 CIPC-treated tip cells. *J Cell Sci* **75**, 131–147 (1985).
980 76. Hachet, O., Bendezú, F. O. & Martin, S. G. Fission yeast: in shape to divide.
981 *Current Opinion in Cell Biology* **24**, 858–864 (2012).
982 77. Martin, S. G., McDonald, W. H., Yates, J. R. & Chang, F. Tea4p Links
983 Microtubule Plus Ends with the Formin For3p in the Establishment of Cell Polarity.
984 *Developmental Cell* **8**, 479–491 (2005).
985 78. Martin, S. G., Rincón, S. A., Basu, R., Pérez, P. & Chang, F. Regulation of the
986 Formin for3p by cdc42p and bud6p. *MBoC* **18**, 4155–4167 (2007).
987 79. Browning, H. *et al.* Tea2p Is a Kinesin-like Protein Required to Generate
988 Polarized Growth in Fission Yeast. *Journal of Cell Biology* **151**, 15–28 (2000).
989 80. Browning, H., Hackney, D. D. & Nurse, P. Targeted movement of cell end
990 factors in fission yeast. *Nat Cell Biol* **5**, 812–818 (2003).
991 81. Busch, K. E., Hayles, J., Nurse, P. & Brunner, D. Tea2p Kinesin Is Involved in
992 Spatial Microtubule Organization by Transporting Tip1p on Microtubules.
993 *Developmental Cell* **6**, 831–843 (2004).
994 82. Kreitzer, G. & Myat, M. M. Microtubule Motors in Establishment of Epithelial
995 Cell Polarity. *Cold Spring Harb Perspect Biol* **10**, a027896 (2018).
996 83. Müsch, A. Microtubule Organization and Function in Epithelial Cells. *Traffic*
997 **5**, 1–9 (2004).
998 84. Rodriguez-Boulan, E. & Macara, I. G. Organization and execution of the

epithelial polarity programme. *Nat Rev Mol Cell Biol* **15**, 225–242 (2014).
85. Sakai, T. *et al.* Armadillo repeat-containing kinesins and a NIMA-related kinase are required for epidermal-cell morphogenesis in Arabidopsis. *The Plant Journal* **53**, 157–171 (2008).
86. Lan, M., Kang, E., Liu, X., Fu, Y. & Zhu, L. Stable ARMADILLO REPEAT KINESIN 2 in light inhibits hypocotyl elongation and facilitates light-induced cortical microtubule reorientation in Arabidopsis. *Journal of Experimental Botany* erac473 (2022) doi:10.1093/jxb/erac473.
87. Malcos, J. L. & Cyr, R. J. An ungrouped plant kinesin accumulates at the preprophase band in a cell cycle-dependent manner. *Cytoskeleton* **68**, 247–258 (2011).
88. Lau, O. S. *et al.* Direct roles of SPEECHLESS in the specification of stomatal self-renewing cells. *Science* **345**, 1605–1609 (2014).
89. Almonacid, M., Terret, M.-E. & Verlhac, M.-H. Nuclear positioning as an integrator of cell fate. *Current Opinion in Cell Biology* **56**, 122–129 (2019).
90. Del Bene, F., Wehman, A. M., Link, B. A. & Baier, H. Regulation of neurogenesis by interkinetic nuclear migration through an apical-basal notch gradient. *Cell* **134**, 1055–1065 (2008).
91. Gundersen, G. G. & Worman, H. J. Nuclear positioning. *Cell* **152**, 1376–1389 (2013).
92. Ashton, N. W. & Cove, D. J. The isolation and preliminary characterisation of auxotrophic and analogue resistant mutants of the moss, Physcomitrella patens. *Molec. Gen. Genet.* **154**, 87–95 (1977).
93. Collonnier, C. *et al.* CRISPR-Cas9-mediated efficient directed mutagenesis and RAD 51-dependent and RAD 51-independent gene targeting in the moss Physcomitrella patens. *Plant Biotechnology Journal* **15**, 122–131 (2017).
94. Yamada, M., Miki, T. & Goshima, G. Imaging Mitosis in the Moss Physcomitrella patens. in *The Mitotic Spindle: Methods and Protocols* (eds. Chang, P. & Ohi, R.) 263–282 (Springer, 2016). doi:10.1007/978-1-4939-3542-0_17.
95. Nakaoka, Y. *et al.* An inducible RNA interference system in Physcomitrella patens reveals a dominant role of augmin in phragmoplast microtubule generation. *Plant Cell* **24**, 1478–1493 (2012).
96. Yi, P. & Goshima, G. Rho of Plants GTPases and Cytoskeletal Elements Control Nuclear Positioning and Asymmetric Cell Division during Physcomitrella patens Branching. *Current Biology* **30**, 2860-2868.e3 (2020).
97. Uchida, M., Ohtani, S., Ichinose, M., Sugita, C. & Sugita, M. The PPR-DYW proteins are required for RNA editing of rps14, cox1 and nad5 transcripts in Physcomitrella patens mitochondria. *FEBS Lett* **585**, 2367–2371 (2011).
98. Galotto, G. *et al.* Myosin XI drives polarized growth by vesicle focusing and local enrichment of F-actin in Physcomitrium patens. *Plant Physiology* **187**, 2509–2529 (2021).

Supplemental movie legends

Movie 1 Overall basal motility of chloroplasts after cell division in *ARKabc-1*
Time-lapse movie of microtubules (mCherry-α-tubulin, magenta) and chloroplasts (autofluorescence, cyan) in apical cells after anaphase onset (0.0 min). The bright

1046 magenta signals on the left represent the anaphase spindles and phragmoplasts. White
1047 arrowheads indicate the positions of the nuclei. Control (expressing mCherry-α-tubulin)
1048 and *ARKabc-1* lines are also shown. Movies were acquired using spinning-disc confocal
1049 microscopy and processed using maximum z-projection (2.5 μm × 3 sections). Scale bar:
1050 20 μm.
1051
1052 **Movie 2 Motility of mitochondria along cytoplasmic microtubules**
1053 Bidirectional movement of a mitochondrion (γF1ATPase-mNG, green) along the
1054 microtubule (mCherry-α-tubulin, magenta). Images were acquired using oblique
1055 illumination fluorescence microscopy. The faint green signals on the left represent
1056 chloroplast autofluorescence. Scale bar: 1 μm.
1057
1058 **Movie 3 Cytoplasmic movement of mNG-RabA2b-marked vesicles**
1059 Time-lapse movie of cytoplasmic movement of RabA2b-marked vesicles (mNG-
1060 RabA2b) in the control, *ARKabc-1* mutant, and rescue lines. Movies were acquired using
1061 spinning-disc confocal microscopy. Autofluorescent chloroplasts are also faintly
1062 visualised. Scale bar: 20 μm.
1063
1064 **Movie 4 mNG-RabA2b-marked vesicles at the protonemal cell tip**
1065 Time-lapse movie of the cluster of mNG-RabA2b-positive vesicles (green) at the cell tip.
1066 Magenta, mCherry-α-tubulin. Autofluorescent chloroplasts in the cytoplasm are also
1067 visible in the green channel. Movies were acquired using spinning-disc confocal
1068 microscopy and processed using maximum z-projection (0.5 μm × 35 sections). Scale
1069 bar: 10 μm.
1070
1071 **Movie 5 Dynamics of cytoplasmic microtubules**
1072 Time-lapse movie of cytoplasmic microtubules (GFP-α-tubulin) in interphase protonemal
1073 cells of control and *ARKabdc-1* lines. Microtubule dynamics were comparable between
1074 these lines (Table S2). Movies were acquired using oblique illumination fluorescence
1075 microscopy. Scale bar: 2 μm.
1076
1077 **Movie 6 Motility of ARKb-mNG on cytoplasmic microtubules**
1078 Time-lapse movie of ARKb-mNG obtained using oblique illumination fluorescence
1079 microscopy. White arrowheads indicate the puncta of ARKb-mNG that move
1080 processively and unidirectionally on the microtubules. Magenta, tubulin; green, ARKb-
1081 mNG. Scale bar: 1 μm.
1082
1083 **Movie 7 *In vitro* motility of ARKb motor on microtubules**
1084 Time-lapse movie of recombinant ARKb (1–613 aa)-GFP on microtubules obtained using
1085 TIRF microscopy (three microtubules are shown). Magenta, tubulin; green, ARKb-GFP.
1086 Scale bar: 5 μm.
1087
1088 **Movie 8 Motor- or tail-deficient ARKb does not suppress chloroplast mispositioning**
1089 **or reduced tip growth in *ARKabc-1* mutant**
1090 Time-lapse movie of protonemal cells expressing truncated or mutated ARKb constructs.
1091 Magenta, mCherry-α-tubulin; cyan, chloroplast. Movies were acquired using an
1092 epifluorescence (wide-field) microscope at a single focal plane. Scale bar: 100 μm.

1093
1094 **Movie 9 RNAi of *ARKd* in *ARKabc-1* causes abnormal outgrowth**
1095 Time-lapse movie of protonemal cells after *ARKd* RNAi induction by β-estradiol
1096 treatment. Left, outgrowth in the apical cell; middle, outgrowth in the subapical cell; right,
1097 no RNAi induction (control). Movies were acquired using a wide-field microscope with
1098 transmission light (20× 0.75 lens). Scale bar: 50 μm.
1099
1100 **Movie 10 Instability of actin foci at the cell tip in *ARKabc-1* mutant**
1101 Time-lapse movie of actin near the cell tip (lifeact-mNG). Movies were acquired using
1102 spinning-disc confocal microscopy and processed using maximum z-projection (0.5 μm
1103 × 7 sections). Scale bar: 5 μm.
1104
1105 **Movie 11 Actin foci disappear with cells expansion**
1106 Time-lapse movie of lifeact-mNG (green) at the cell tip. Four cells are shown. Magenta,
1107 mCherry-α-tubulin. Autofluorescent chloroplasts in the cytoplasm are also visible in the
1108 green channel. Movies were acquired using spinning-disc confocal microscopy and
1109 processed using maximum z-projection (1 μm × 23 sections). Scale bar: 10 μm.
1110
1111 **Movie 12 RopGEF3 at the protonemal cell tip**
1112 Time-lapse movie of RopGEF3-3×mNG (green) at the cell tip. Magenta, mCherry-α-
1113 tubulin. Autofluorescent chloroplasts in the cytoplasm are also visible in the green
1114 channel. Movies were acquired using a spinning-disc confocal microscope with a z-series
1115 taken every 0.5 μm for a range of 17 μm. The best focal plane is presented. Scale bar: 10
1116 μm.
1117
1118 **Movie 13 RopGEF6 at the protonemal cell tip**
1119 Time-lapse movie of RopGEF6-3×mNG (green) at the cell tip. Magenta, mCherry-α-
1120 tubulin. Autofluorescent chloroplasts in the cytoplasm are also visible in the green
1121 channel. Movies were acquired using a spinning-disc confocal microscope with a z-series
1122 taken every 0.5 μm for a range of 17 μm. The best focal plane is presented. Scale bar: 10
1123 μm.
1124
1125 **Movie 14 For2A at the protonemal cell tip**
1126 Time-lapse movie of For2A-mNG (green) at the cell tip. Magenta, mCherry-α-tubulin.
1127 Note that autofluorescent chloroplasts in the cytoplasm are also visible in the green
1128 channel. Movies were acquired using a spinning-disc confocal microscope with a z-series
1129 taken every 0.5 μm for a range of 17 μm. The best focal plane is presented. Scale bar: 10
1130 μm.
1131
1132 **Movie 15 Dynamics of filamentous actin in the endoplasm**
1133 Time-lapse movie of filamentous actin (lifeact-mNG) in interphase protonemal cells
1134 obtained using oblique illumination fluorescence microscopy. Tracking of individual F-
1135 actin ends revealed a slightly reduced growth rate in the mutant line (Fig. 5F). Scale bar:
1136 5 μm.
1137
1138 **Movie 16 Apical RopGEF3 signals diminish with cell expansion**

1139 Time-lapse movie of RopGEF3-3×mNG (green) at the cell tip. Three cells are shown.
1140 Magenta, mCherry-α-tubulin. Autofluorescent chloroplasts in the cytoplasm are also
1141 visible in the green channel. Movies were acquired using spinning-disc confocal
1142 microscopy and processed using maximum z-projection (1 μm × 23 sections). Scale bar:
1143 10 μm.
1144
1145 **Movie 17 Apical RopGEF6 signals diminish with cell expansion**
1146 Time-lapse movie of RopGEF6-3×mNG (green) at the cell tip. Three cells are shown.
1147 Magenta, mCherry-α-tubulin. Autofluorescent chloroplasts in the cytoplasm are also
1148 visible in the green channel. Movies were acquired using spinning-disc confocal
1149 microscopy and processed using maximum z-projection (1 μm × 23 sections). Scale bar:
1150 10 μm.
1151
1152 **Movie 18 Apical For2A signals diminish with cell expansion**
1153 Time-lapse movie of For2A-mNG (green) at the cell tip. Three cells are shown. Magenta,
1154 mCherry-α-tubulin. Autofluorescent chloroplasts in the cytoplasm are also visible in the
1155 green channel. Movies were acquired using spinning-disc confocal microscopy and
1156 processed using maximum z-projection (1 μm × 23 sections). Scale bar: 10 μm.
1157
1158 ## Supplemental tables
1159
1160 **Table S1 Mutant alleles used in this study**
1161
1162 **Table S2 Statistical analysis of microtubule dynamics in *ARK* mutants**
1163
1164 **Table S3 Statistical analysis of microtubule dynamics in moss lines expressing**
1165 **AtARK2 or AtARK3**
1166
1167 **Table S4 Moss lines used in this study**
1168
1169 **Table S5 Plasmids used in this study**
1170
1171 **Table S6 Primers used for plasmid construction and sequencing**
1172
1173 **Table S7 Primers used for genotyping PCR**

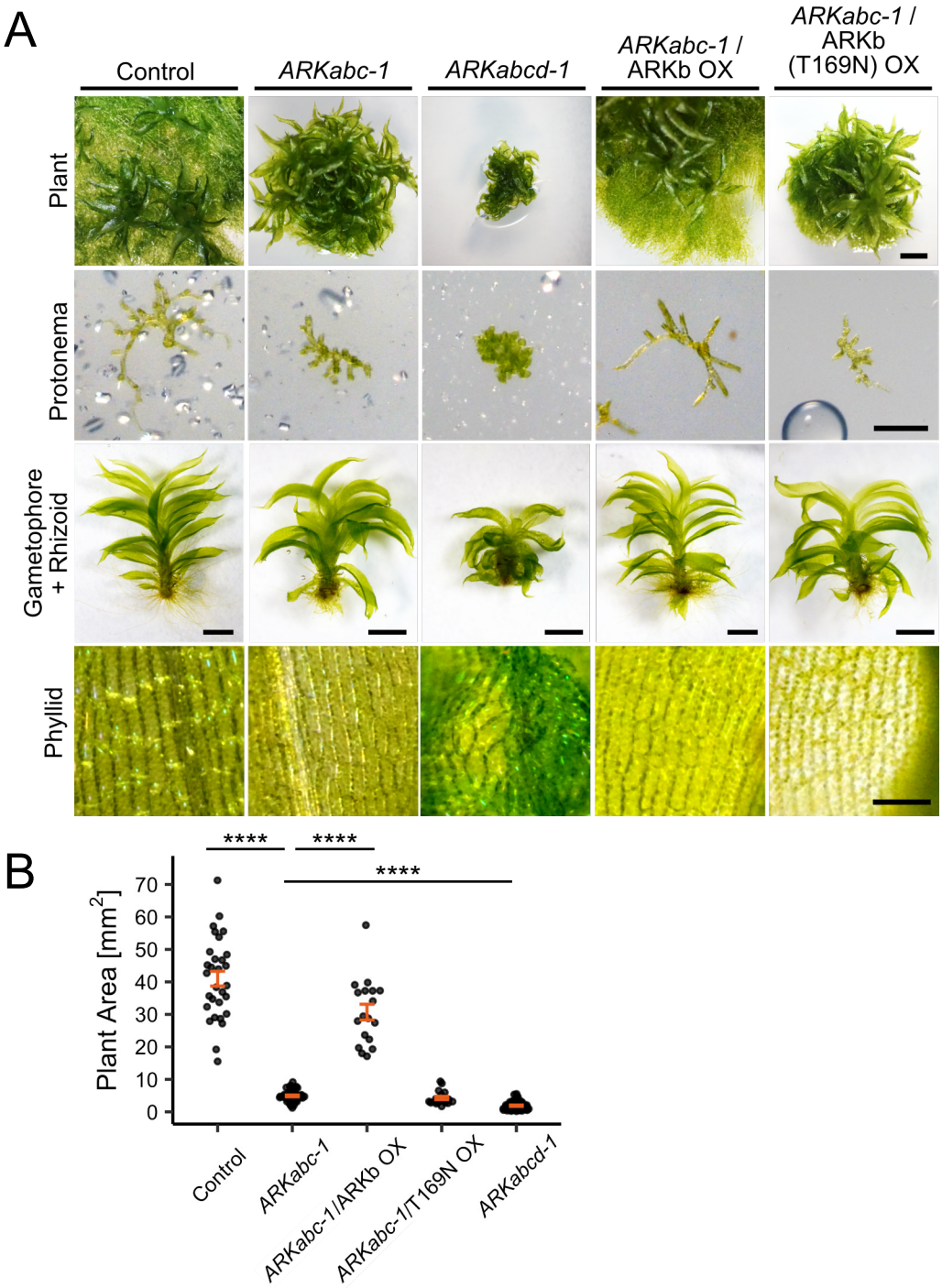

Fig. 1 *ARK* disruption causes severe growth defects

(A) Representative images of 5-week-old moss on the culture plate, which was regenerated from a single protoplast (top row), 6-day-old protonemata (second row), gametophores and rhizoids (third row), and the phyllid surface (bottom row). The mosses used in this experiment were control (mCherry-α-tubulin), *ARKabc-1*, *ARKabcd-1*, and overexpression/rescue lines (*ARKabc-1*/ARKb-mNG OX and *ARKabc-1*/ARKb (T169N) -mNG OX). Scale bars: 1 mm (top row), 200 μm (second row), 1 mm (third row), and 100 μm (bottom).

(B) Plant area comparison. Plants were cultured from a single protoplast for three weeks on BCDAT medium. The same moss lines as those in (A) were used in this experiment. The mean area (mm^2) was 41.0 ± 2.28 (control, ±SEM, n = 30), 4.91 ± 0.267 (*ARKabc-1*, ±SEM, n = 45), 30.7 ± 2.42 (*ARKabc-1*/ARKb-mNG OX, ±SEM, n = 18), 4.26 ± 0.501 (*ARKabc-1*/ARKb (T169N) -mNG OX, ±SEM, n = 18), 1.90 ± 0.188 (*ARKabcd-1*, ±SEM, n = 49). P-values were calculated using Steel-Dwass test; $P < 0.0000001$ (control - *ARKabc-1*), $P = 0.0000001$ (*ARKabc-1* - *ARKabc-1*/ARKb-mNG OX), $P < 0.0000001$ (*ARKabc-1* - *ARKabcd-1*).

2

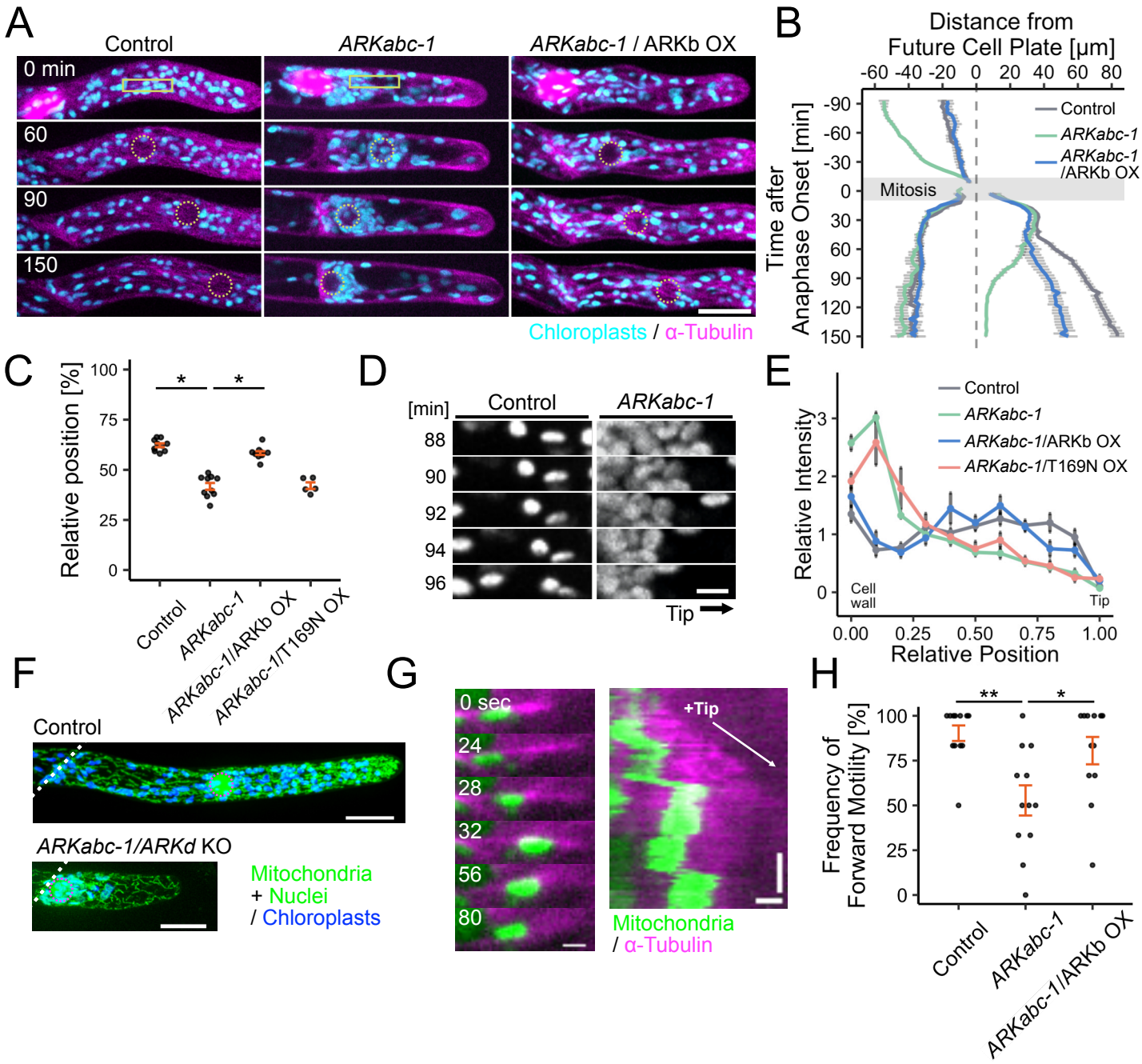

Fig. 2 ARK transports multiple organelles in protonemal cells

(A) Movement of the nuclei and chloroplasts in protonemal apical cells. The onset time of anaphase was set to 0 min. The yellow circles indicate the positions of the nuclei. Yellow boxes are highlighted in (D). Images were acquired using spinning-disc confocal microscopy and processed using maximum z-projection: 2.5 μm × 3 sections (control mCherry-α-Tubulin line and *ARKabc-1)* or 5 μm × 3 sections (*ARKabc-1*/ARKb-mNG OX). Scale bar: 20 μm.

(B) Nuclear movement before and after apical cell division. The temporal change in the distance between the nucleus and the cell plate (set at position 0) was plotted with SEM. *n* = 9 cells (control), *n* = 10 cells (*ARKabc-1*), *n* = 10 cells (*ARKabc-1*/ARKb-mNG OX).

(C) Comparison of the relative position of the metaphase plate of the spindle in dividing apical cells. The relative position was determined by dividing the distance between the metaphase plate and the basal cell wall by that between the cell tip and the basal cell wall. mCherry-α-tubulin was used as the control. The mean relative position was 62.2 ± 0.930% (control, ±SEM, *n* = 10), 41.7 ± 1.71% (*ARKabc-1*, ±SEM, *n* = 10), 58.3 ± 0.880% (*ARKabc-1*/ARKb-mNG OX, ±SEM, *n* = 11), 42.1 ± 1.67% (*ARKabc-1*/ARKb (T169N)-mNG OX, ±SEM, *n* = 5). P-values were calculated using Steel-Dwass test; P = 0.0353 (control - *ARKabc-1*), P = 0.0252 (*ARKabc-1* - *ARKabc-1*/ARKb-mNG OX), P = 1.00 (*ARKabc-1* - *ARKabc-1*/ARKb (T169N)-mNG OX).

(D) Movement of individual chloroplasts 88–96 min after anaphase onset. Yellow boxes in (A) are highlighted. Images were acquired using spinning-disc confocal microscopy and processed using maximum z-projection (2.5 μm × 3 sections). Scale bar: 5 μm.

(E) Relative intensity of chloroplasts in apical cells 150 min after anaphase onset. Chloroplast accumulation near the basal cell wall was observed in *ARKabc-1* (*n* = 14), *ARKabc-1*/ARKb-mNG OX (*n* = 12) and *ARKabc-1*/ARKb (T169N)-mNG OX (*n* = 9). mCherry-α-tubulin was used as the control (*n* = 13). The quantification methods are described in the Methods section.

(F) Distribution of mitochondria in apical cells. Magenta circles indicate the positions of the nuclei. Images were acquired using a spinning-disc confocal microscope and processed using maximum z-projection: 0.5 μm × 47 (control) or 55 (*ARKabc-1*) sections. Scale bars: 20 μm.

(G) Bidirectional motility of mitochondria on a microtubule in the control line (mCherry-α-Tubulin/γ-F1ATPase-mNG). The right panel shows the kymograph. The growing microtubule end (i.e. the plus end) is indicated by an arrow. Images were acquired using oblique illumination fluorescent microscopy. Scale bars: 1 μm (horizontal) and 30 s (vertical).

(H) Frequency of tip-directed motility of mitochondria in apical cells. The quantification method has been described in the Methods section. The mean frequency was 90.3 ± 4.33% (control, ± SEM, n = 12 cells), 52.8 ± 8.42% (*ARKabc-1*, ± SEM, n = 12 cells), 80.6 ± 7.63% (*ARKabc-1*/ARKb OX, ± SEM, n = 12 cells). P-values were calculated using Steel-Dwass test; P = 0.0015 (control - *ARKabc-1*), P = 0.0453 (*ARKabc-1* - *ARKabc-1*/ARKb OX).

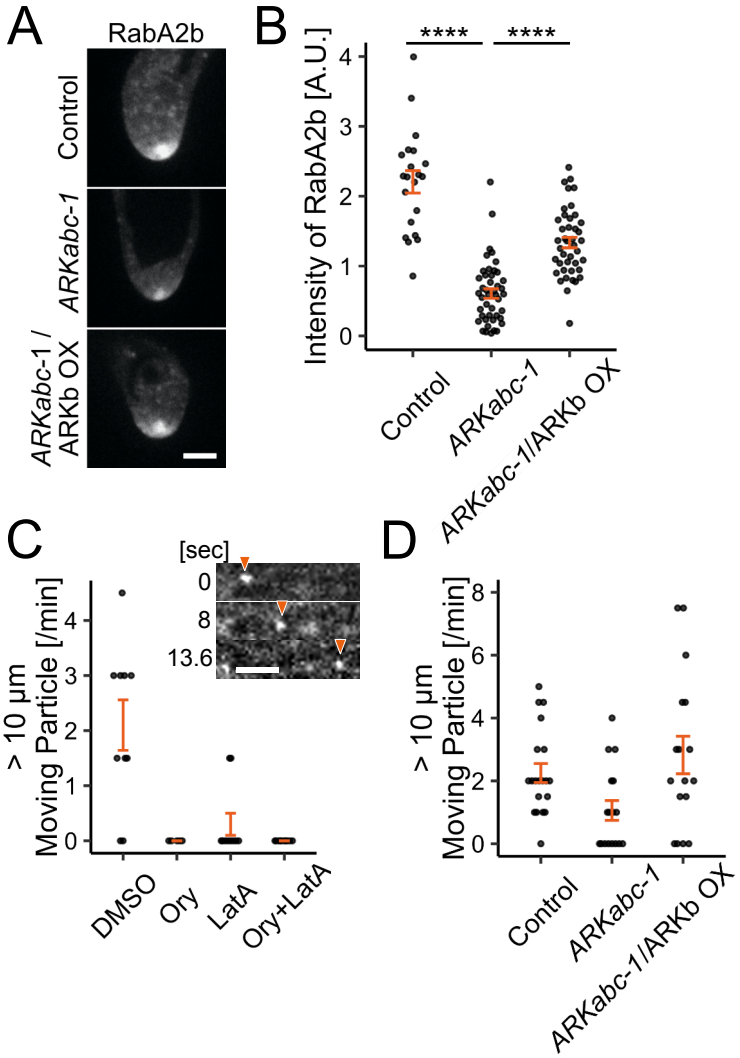

Fig. 3 ARK promotes the movement of RabA2b-marked secretory vesicles

(A) and (B) Accumulation of mNG-RabA2b at the cell tip was reduced in *ARKabc-1*. mCherry-α-tubulin/RabA2b-mNG was used as control. Images were acquired using a spinning-disc confocal microscope with a z-series taken every 0.5 µm for a range of 15 µm. The best focal plane is presented. Scale bar: 5 µm. The mean intensity in (B) was 2.21 ± 0.160 (control, ±SEM, *n* = 21), 0.606 ± 0.0679 (*ARKabc-1*, ±SEM, *n* = 45), and 1.32 ± 0.0747 (*ARKabc-1*/ARKb-mNG OX, ±SEM, *n* = 42). P-values were calculated using Steel-Dwass test; P < 0.0000001 (control - *ARKabc-1*), P < 0.0000001 (*ARKabc-1* - *ARKabc-1*/ARKb-mNG OX).

(C) Representative images of RabA2b-positive vesicles (arrowheads) and number of motile RabA2b-positive vesicles in the absence of microtubules or actin. Scale bar: 5 µm. Images were acquired using a spinning-disc confocal microscope. The number of mNG puncta moving >10 µm in a minute was counted in each cell. The mean number was 2.1 ± 0.46 (control, ±SEM, *n* = 10 cells), 0.0 ± 0.0 (10 µM oryzalin, ±SEM, *n* = 5 cells), 0.3 ± 0.20 (25 µM latrunculin A, ±SEM, *n* = 10 cells), 0.0 ± 0.0 (10 µM oryzalin + 25 µM latrunculin A, ±SEM, *n* = 10 cells).

(D) Number of RabA2b-positive vesicles moving for >10 µm in a minute. mCherry-α-tubulin/RabA2b-mNG was used as control. The mean number was 2.3 ± 0.30 (control, ±SEM, *n* = 20 cells), 1.1 ± 0.31 (*ARKabc-1*, ± SEM, *n* = 17 cells), 2.8 ± 0.60 (*ARKabc-1*/ARKb-mNG OX, ±SEM, *n* = 17 cells). P-values were calculated using Steel-Dwass test; P = 0.1006 (control - *ARKabc-1*), P = 0.2532 (*ARKabc-1* - *ARKabc-1*/ARKb-mNG OX).

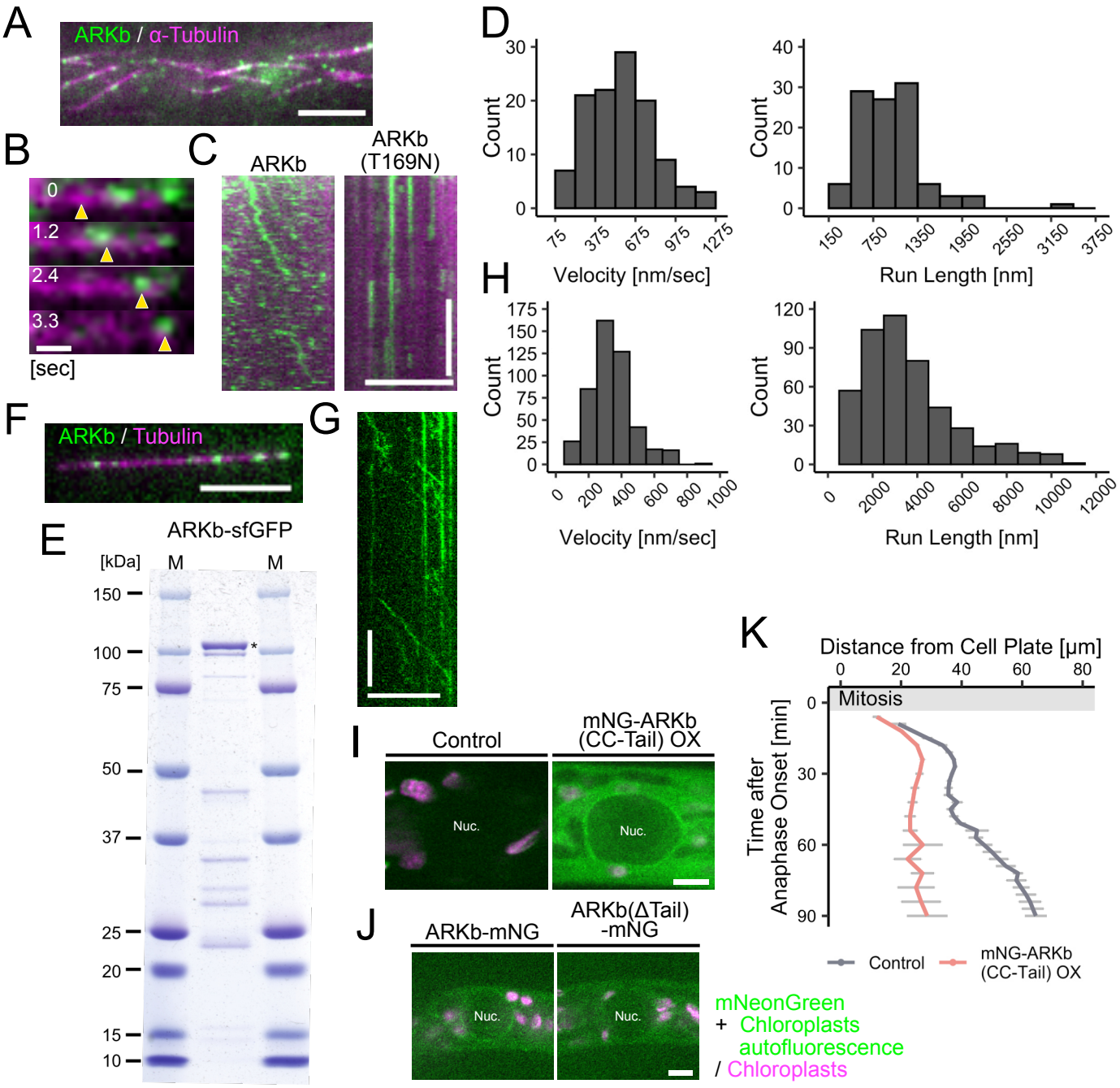

Fig. 4 ARKb shows processive motility and is enriched around the nucleus in a tail-dependent manner

(A) Localisation ARKb–mNG on endoplasmic microtubules in protonemal cells. Giant green signals near the scale bar represent autofluorescent chloroplasts. Scale bar: 5 μm. Images were acquired using oblique illumination fluorescence microscopy.
(B) Processive ARKb–mNG movement along the microtubule *in vivo*. Arrowheads indicate ARKb-mNG signals. Scale bar: 500 nm.
(C) Kymographs of ARKb-mNG (left) and ARKb (T169N)-mNG (right) on microtubules *in vivo*. Scale bars: 5 μm (horizontal) and 5 s (vertical).
(D) Velocity and run length of moving ARKb-mNG signals *in vivo*. Mean values: 572 ± 243 nm/s (velocity, mean ±SD, n = 115) and 986 ± 416 nm (run length, mean ±SD, n = 106).
(E) Coomassie staining of purified ARKb-sfGFP.
(F) Localisation of a single ARKb-sfGFP motor on a single microtubule *in vitro*. Scale bar: 5 μm. Images were acquired with TIRF microscopy.
(G) Kymograph of ARKb-sfGFP on a microtubule in a single kinesin motility assay. Scale bars: 10 μm (horizontal) and 20 s (vertical).
(H) Velocity and run length of moving ARKb-sfGFP signals in a single kinesin motility assay. Mean values: 340 ± 138 nm/s (velocity, mean ±SD, n = 481) and 3.13 ± 2.17 μm (run length, mean ±SD, n = 172).
(I) Motor-deleted ARKb (mNG-CC-Tail) localisation. The region devoid of mNG signals indicates the position of the nucleus. The control cell does not express mNG. Images were acquired with a spinning-disc confocal microscope using a z-series taken every 1 μm for a range of 16 μm. The best focal plane is presented. Scale bar: 5 μm.
(J) ARKb-mNG (left) and tail-deleted ARKb-mNG (right) localisation in the absence of endoplasmic microtubules. Microtubules were depolymerised using 10 μM oryzalin. The region devoid of mNG signals indicates the position of the nucleus. Images were acquired with a spinning-disc confocal microscope using a z-series taken every 1 μm for a range of 14 μm. The best focal plane is presented. Scale bar: 5 μm.
(K) Nuclear movement after apical cell division. The temporal change in the distance between the nucleus and the cell plate (set at position 0) was plotted with SEM (n = 5 each). The control data are identical to those shown in Fig. 2B.

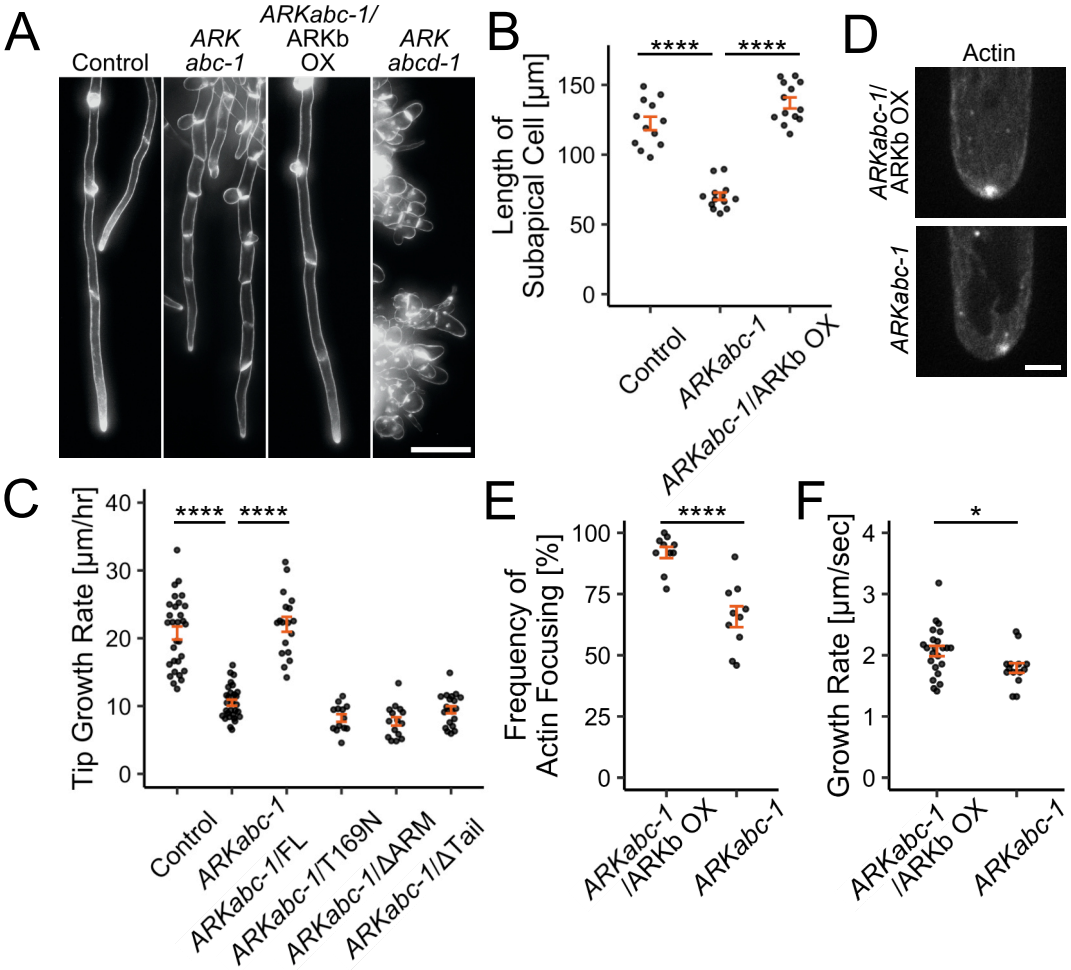

Fig. 5 Cell tip growth was severely suppressed in the absence of ARK

(A) Representative images of protonemal cells. The plasma membrane was visualised using FM4-64. The mCherry-α-tubulin line was used as the control. *ARKabcd-1* exhibited additional nuclear signals derived from the mCherry-tagged histone. Images were obtained using epifluorescence (wide-field) microscopy and processed using maximum z-projection of 5 µm × 31 sections. Scale bars, 100 µm.

(B) Comparison of subapical cell length. The mean length was 122 ± 4.83 µm (control, ±SEM, *n* = 12), 70.2 ± 2.67 µm (*ARKabc-1*, ±SEM, *n* = 13), 137 ± 3.97 µm (*ARKabc-1*/ARKb-mNG OX, ±SEM, *n* = 13). P-values were calculated using Tukey's multiple comparison test; P < 0.0000001 (control - *ARKabc-1*), P < 0.0000001 (*ARKabc-1* - *ARKabc-1*/ARKb-mNG OX).

(C) Comparison of tip growth rates of caulonemal filament. The mCherry-α-tubulin line was used as the control. The mean rate was 20.8 ± 0.962 µm/h (control, ±SEM, *n* = 30), 10.5 ± 0.455 µm/h (*ARKabc-1*, ±SEM, *n* = 29), 22.1 ± 1.10 µm/h (*ARKabc-1*/ARKb-mNG OX, ±SEM, *n* = 18), 8.23 ± 0.56 µm/h (*ARKabc-1*/ARKb (T169N) -mNG OX, ±SEM, *n* = 13). P-values were calculated by Games-Howell test; P < 0.0000001 (control - *ARKabc-1*), P = 0.0000003 (*ARKabc-1* - *ARKabc-1*/ARKb-mNG OX).

(D) Representative images of actin foci at the cell tip. Images were acquired using a spinning-disc confocal microscope with a z-series taken every 0.5 µm for a range of 18 µm. The best focal plane is presented. Scale bar: 5 µm.

(E) Frequency of actin focusing. The mean frequencies were 65.7 ± 4.26% (*ARKabc-1*, ±SEM, *n* = 10) and 92.0 ± 2.29% (*ARKabc-1* / ARKb-mNG OX, ±SEM, *n* = 10). The P-value was calculated using Student's two-sample t-test: P = 0.00003761 (*ARKabc-1* - *ARKabc-1*/ARKb-mNG OX).

(F) Comparison of actin growth rates near the cell tip. F-actin was visualised using Lifeact-mNG. The mean rate was 1.79 ± 0.0790 µm/s (*ARKabc-1*, ±SEM, *n* = 14), 2.07 ± 0.084 µm/s (*ARKabc-1*/ARKb-mNG OX, ±SEM, *n* = 23). The P-value was calculated using Student's two-sample t-test: P = 0.03291 (*ARKabc-1* - *ARKabc-1*/ARKb-mNG OX).

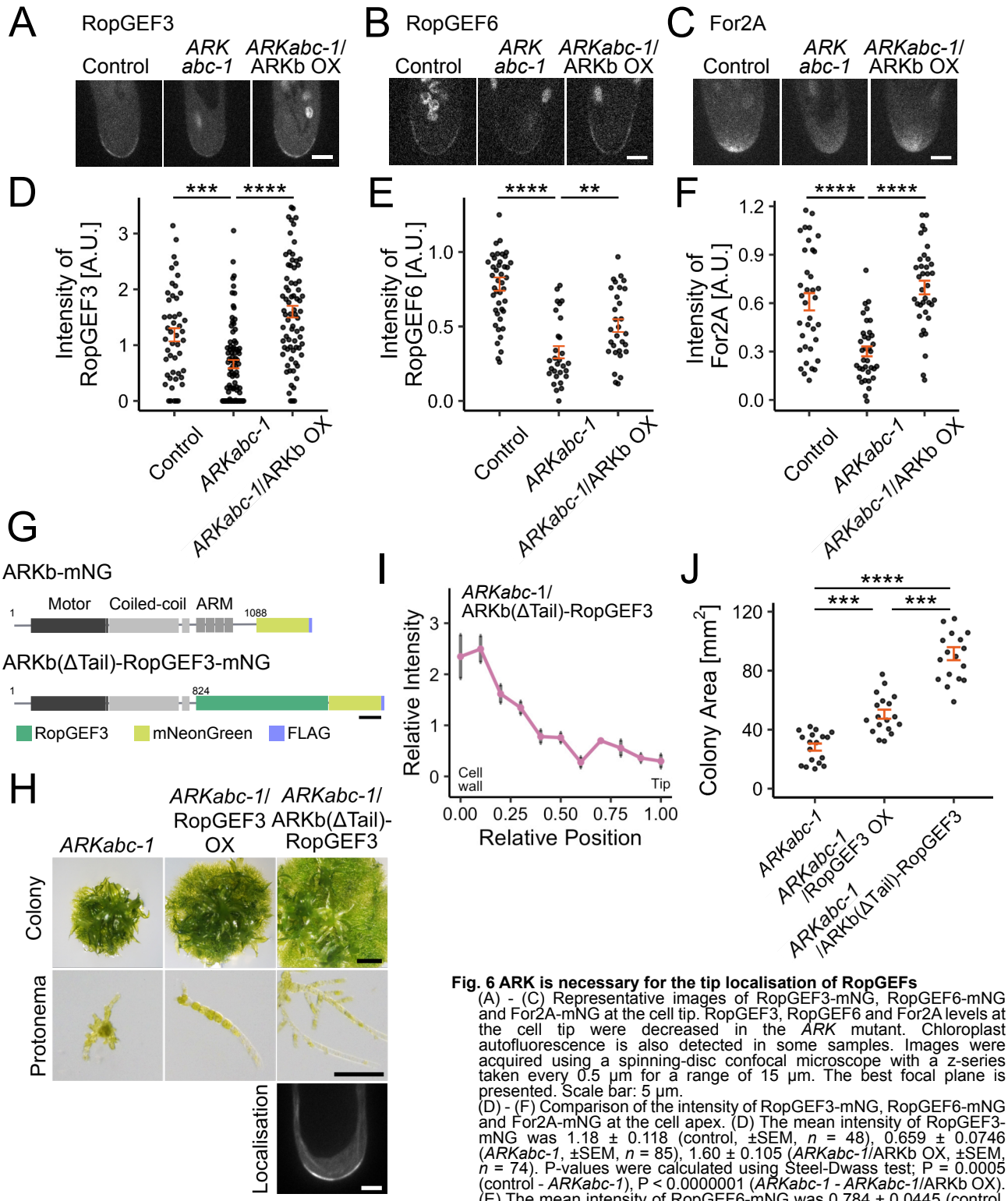

Fig. 6 ARK is necessary for the tip localisation of RopGEFs

(A) - (C) Representative images of RopGEF3-mNG, RopGEF6-mNG and For2A-mNG at the cell tip. RopGEF3, RopGEF6 and For2A levels at the cell tip were decreased in the *ARK* mutant. Chloroplast autofluorescence is also detected in some samples. Images were acquired using a spinning-disc confocal microscope with a z-series taken every 0.5 µm for a range of 15 µm. The best focal plane is presented. Scale bar: 5 µm.

(D) - (F) Comparison of the intensity of RopGEF3-mNG, RopGEF6-mNG and For2A-mNG at the cell apex. (D) The mean intensity of RopGEF3-mNG was 1.18 ± 0.118 (control, ±SEM, n = 48), 0.659 ± 0.0746 (*ARKabc-1*, ±SEM, n = 85), 1.60 ± 0.105 (*ARKabc-1*/ARKb OX, ±SEM, n = 74). P-values were calculated using Steel-Dwass test; P = 0.0005 (control - *ARKabc-1*), P < 0.0000001 (*ARKabc-1* - *ARKabc-1*/ARKb OX). (E) The mean intensity of RopGEF6-mNG was 0.784 ± 0.0445 (control, ±SEM, n = 43), 0.327 ± 0.0409 (*ARKabc-1*, ±SEM, n = 29), 0.506 ± 0.0432 (*ARKabc-1*/ARKb OX, ±SEM, n = 30). P-values were calculated using Steel-Dwass test; P < 0.0000001 (control - *ARKabc-1*), P = 0.0076 (*ARKabc-1* - *ARKabc-1*/ARKb OX). (F) The mean intensity of For2A-mNG was 0.609 ± 0.0537 (control, ±SEM, n = 36), 0.301 ± 0.0304 (*ARKabc-1*, ±SEM, n = 36), 0.697 ± 0.0423 (*ARKabc-1*/ARKb OX, ±SEM, n = 36). P-values were calculated using Games-Howell test; P = 0.0000192 (control - *ARKabc-1*), P < 0.0000001 (*ARKabc-1* - *ARKabc-1*/ARKb OX).

(G) Motor-RopGEF-fusion construct used in this study. Tailless ARKb and mNeonGreen-FLAG were fused to the N-terminal and C-terminal sides of RopGEF3, respectively. Scale bar: 100 amino acids.

(H) Representative images of *ARKabc-1* moss expressing native or motor-fused RopGEF3 (ARKb(ΔTail)-RopGEF3-mNG). Top row: 5-week-old moss grown from a single protoplast; second row: 6-day-old protonemata; third row: tip localisation of the fusion protein. Scale bars: 2 mm (top row), 200 µm (second row), and 5 µm (third row). The fluorescent image was acquired using a spinning-disc confocal microscope with a z-series taken every 0.5 µm for a range of 15 µm. The best focal plane is presented. Scale bar: 5 µm.

(I) Relative intensity of chloroplasts along the apical cell at 150 min after anaphase onset. Chloroplast accumulation near the basal cell wall observed in *ARKabc-1* was not rescued by the fusion RopGEF3 construct (n = 6).

(J) Area comparison of 5-week-old moss on the BCDAT culture plate (from a single protoplast). The mean area (mm²) was 28.2 ± 2.42 (*ARKabc-1*, ±SEM, n = 18), 50.5 ± 3.08 (*ARKabc-1*/RopGEF3-mNG OX, ±SEM, n = 18), 91.5 ± 4.41 (*ARKabc-1*/ARKb(Δtail)-RopGEF3-mNG, ±SEM, n = 18). P-values were calculated using Steel-Dwass test; P = 0.0004 (*ARKabc-1* - *ARKabc-1*/RopGEF3-mNG OX), P = 0.0000106 (*ARKabc-1* - *ARKabc-1*/ARKb-RopGEF3-mNG), P = 0.0001 (*ARKabc-1*/RopGEF3-mNG OX - *ARKabc-1*/ARKb-RopGEF3-mNG).

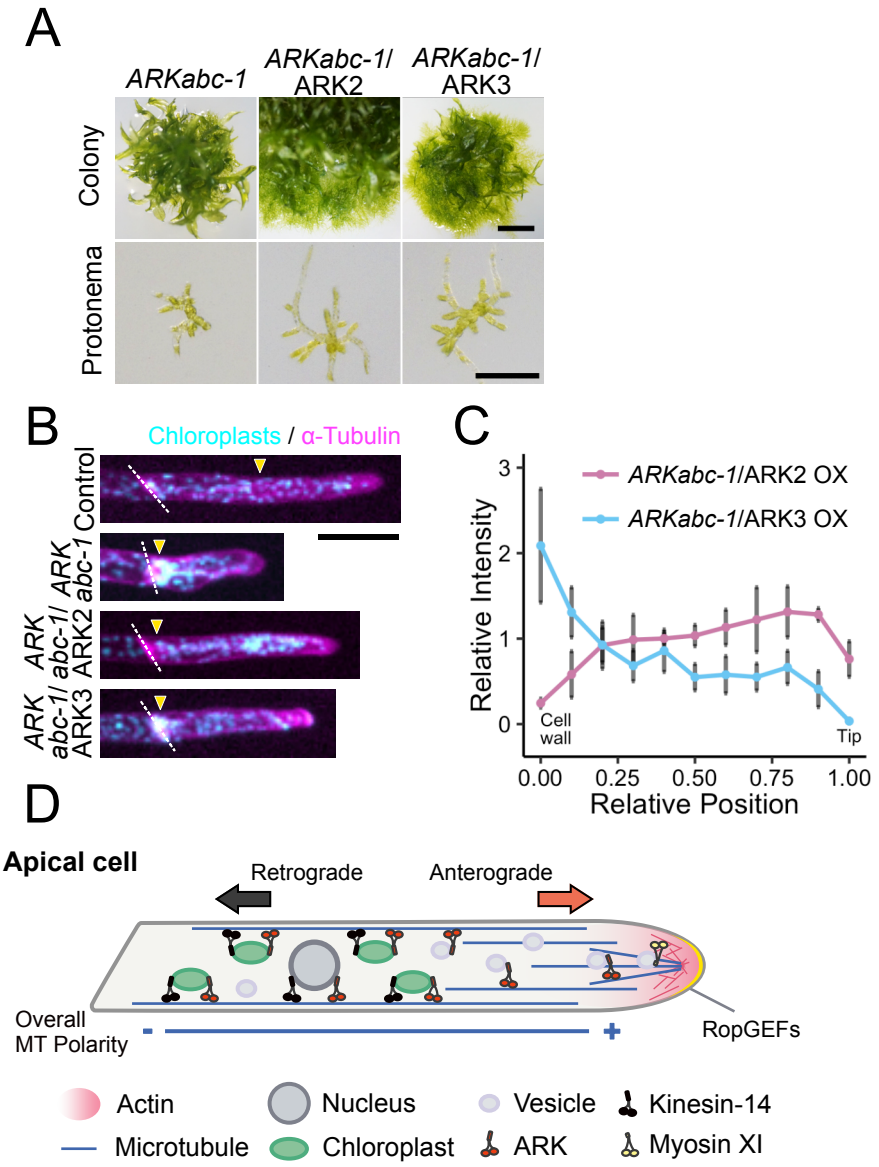

Fig. 7 AtARK2 and AtARK3 expression partially rescues moss *ARKabc-1*

(A) Representative images of 5-week-old moss regenerated from a single protoplast (top) and 6-day-old protonemata (bottom). Scale bars: 2 mm (top) and 200 µm (bottom).

(B) Representative images of protonemal apical cells. Arrowheads and white lines indicate the positions of the nucleus and the cell plate, respectively. Scale bar: 100 µm. Images were acquired with epifluorescence (wide-field) microscopy (single focal plane).

(C) Relative intensity of chloroplasts along the apical cell at 150 min after anaphase onset (±SEM). The basal accumulation of chloroplasts in *ARKabc-1* was abolished after the ectopic expression of AtARK2 (n = 9) but not of AtARK3 (n = 10).

(D) Model for microtubule-dependent transport in *Physcomitrium patens* protonemal cells. Giant organelles, such as nuclei and chloroplasts, are transported to the plus and minus ends of the microtubules by ARK and kinesin-14s (KCH and KCBP), respectively (i.e. tug-of-war). ARK also transports secretory vesicles, which are presumably passed to myosin XI at the cell tip for exocytosis [36]. The proteins and cell wall materials required for tip growth are also candidate cargos for ARK, as ARK depletion severely suppresses polarised cell growth.

S1

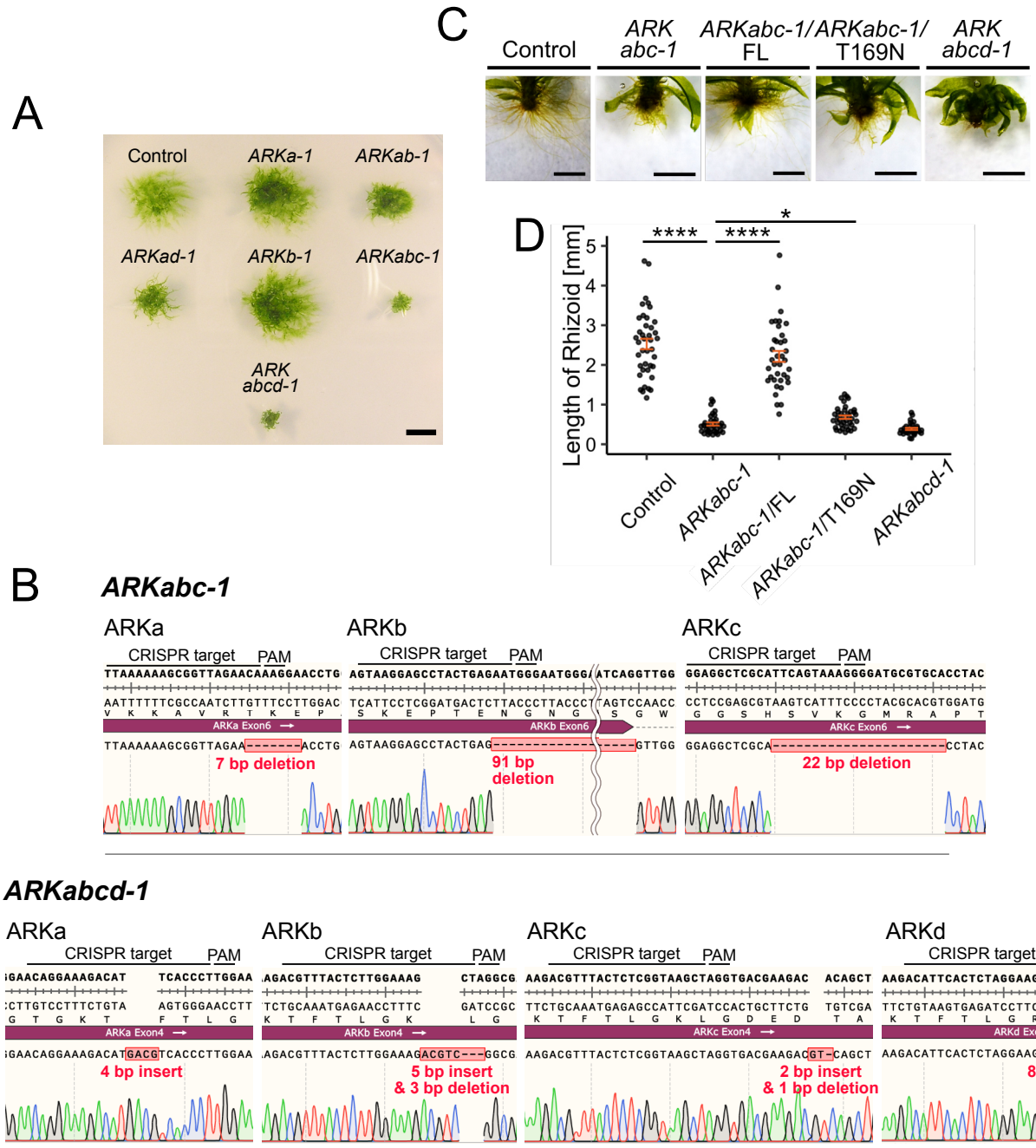

Supplemental Fig. 1 Establishment of *Physcomitrium patens ARK* mutants

(A) Representative images of 3-week-old *ARK* mutants. mCherry-α-tubulin was used as a control. Scale bar: 5 mm.

(B) Sequencing revealed frameshift mutations in the *ARKabc-1* and *ARKabcd-1* sequences used in this study (displayed as SnapGene sequence files). The altered amino acid sequences are shown in Table S1.

(C) Rhizoid images. The images presented in Fig. 1A are cropped and magnified. Scale bar: 1 mm.

(D) Rhizoid length comparison. The mean length (mm) was 2.53 ± 0.132 (control, ±SEM, n = 40), 0.510 ± 0.0406 (*ARKabc-1*, ±SEM, n = 34), 2.21 ± 0.138 (*ARKabc-1*/ARKb-mNG full-length OX, ±SEM, n = 37), 0.683 ± 0.0427 (*ARKabc-1*/ARKb (T169N) -mNG OX, ±SEM, n = 38), 0.387 ± 0.0275 (*ARKabcd-1*, ±SEM, n = 30). P-values were calculated using Steel-Dwass test; P < 0.0000001 (control - *ARKabc-1*), P < 0.0000001 (*ARKabc-1* - *ARKabc-1*/ARKb-mNG OX), P = 0.0295 (*ARKabc-1* - *ARKabc-1*/ARKb(T169N)-mNG OX). P = 0.3144 (*ARKabc-1* - *ARKabcd*-1).

S2

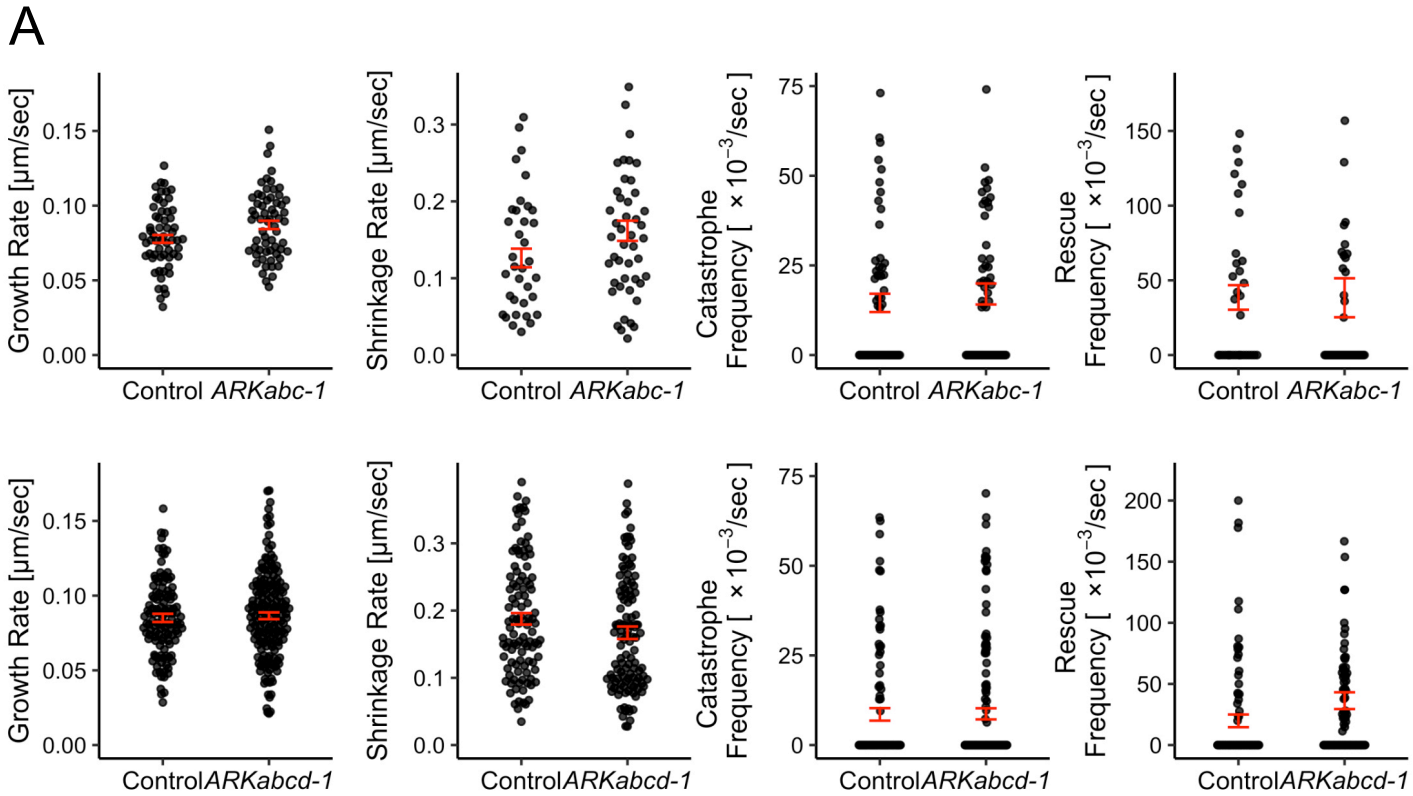

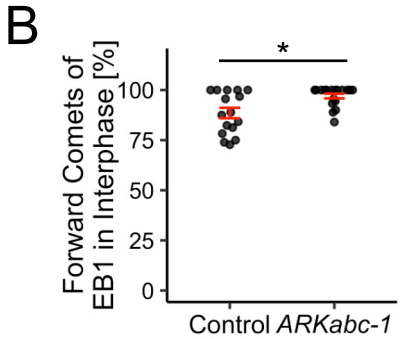

Supplemental Fig. 2 *ARK* deletion does not affect microtubule dynamics

(A) Comparison of microtubule dynamics. Upper row, control (mCherry-α-tubulin) and *ARKabc-1*; lower row, control (GFP-α-tubulin/Histone-mCherry), and *ARKabcd-1*. The mean ± SEM, number of samples, and P-values are shown in Table S2.

(B) Comparison of microtubule orientation in apical cells based on EB1-Citrine tracking. The quantification method is described in the Methods section. The frequency of tip-directed movement (%) was 88.5 ± 2.61 (mCherry-α-Tubulin, ±SEM, n = 16) and 97.0 ± 1.16 (*ARKabc-1*, ±SEM, n = 18). The P-value was calculated using Mann-Whitney U test; P = 0.0366.

S3

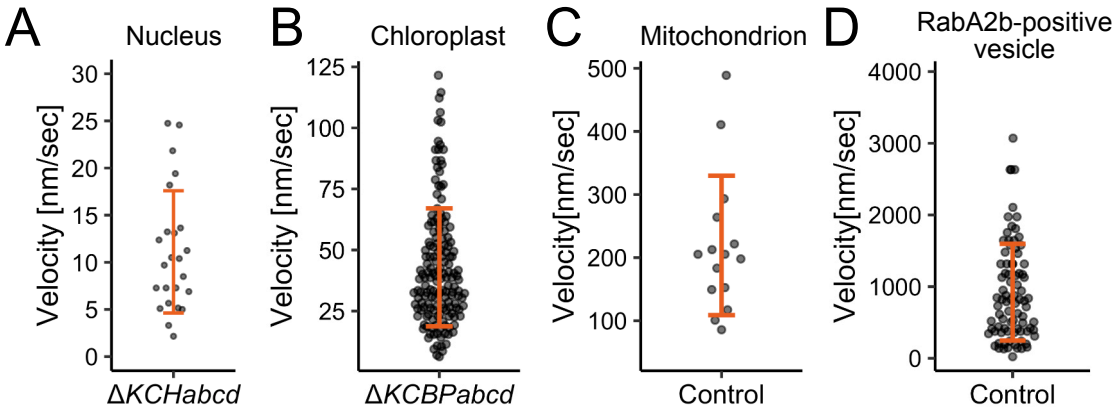

Supplemental Fig. 3 Organelle motility rate

(A) Rate of nuclear motility in apical cells of the Δ*KCHabcd* line. Mean rate: 11.1 ± 6.49 nm/s (±SD, n = 24).

(B) Rate of chloroplast motility in apical cells of Δ*KCBPabcd* line. The mean rate was 42.9 ± 24.2 nm/s (apical direction, ±SD, n = 160).

(C) Rate of mitochondrial motility in apical cells of the control line (mCherry-α-tubulin). The mean rate was 219 ± 110 nm/s (apical direction, ±SD, n = 15).

(D) Rate of motility of RabA2b-positive vesicle in apical cells of the control line (mCherry-α-tubulin). The mean rate was 922 ± 674 nm/s (apical direction, ±SD, n = 85).

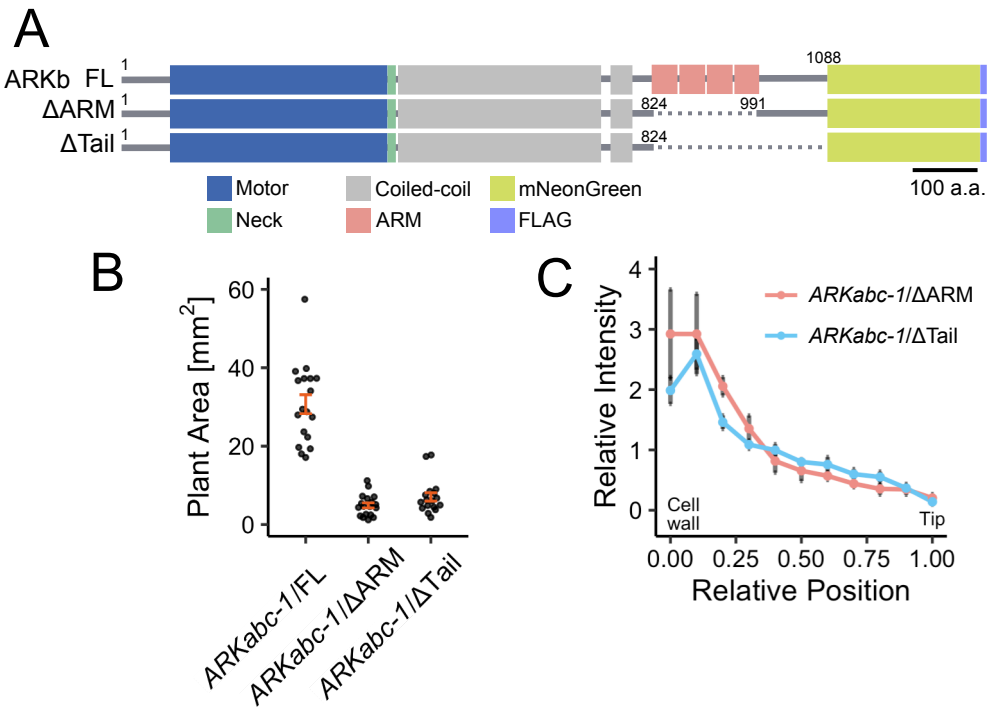

Supplemental Fig. 4 The truncation-rescue assay reveals the essentiality of ARM repeats

(A) Truncated ARKb-mNG constructs used in this experiment. The protein domains were predicted using NCBI's conserved domain database (https://www.ncbi.nlm.nih.gov/Structure/cdd/wrpsb.cgi) and SMART (http://smart.embl.de).

(B) Area comparison of 3-week-old moss. A single protoplast was cultured for three weeks on BCDAT medium. The datasets of *ARKabc-1*/FL (full-length) are identical to those shown in Fig. 1B. The mean area (mm^2) was 4.88 ± 0.651 (*ARKabc-1*/ΔARM, ±SEM, n = 18), 7.04 ± 1.07 (*ARKabc-1*/ΔTail, ±SEM, n = 18).

(C) Relative intensity of chloroplasts along the apical cell at 150 min after anaphase onset. The chloroplasts remained accumulated near the basal cell wall after the expression of the ΔARM (n = 7) or ΔTail (n = 12) construct.

S5

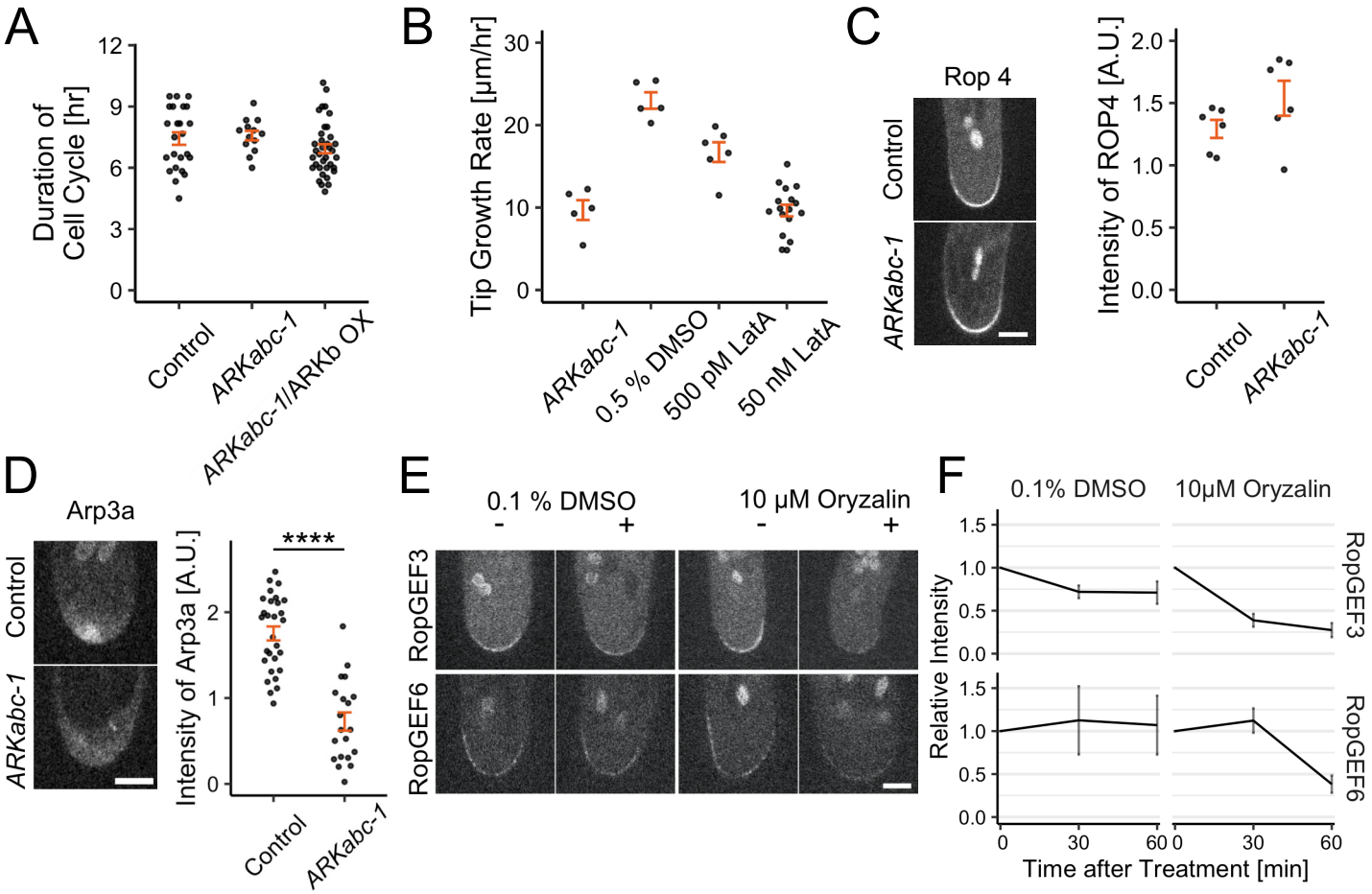

Supplemental Fig. 5 *ARK* deletion affects cell length and Arp3a localisation, but not the cell cycle duration or Rop4 localisation

(A) Comparison of cell cycle durations. The mean duration (h) was 7.43 ± 0.307 (control, ±SEM, n = 24), 7.58 ± 0.232 (*ARKabc-1*, ±SEM, n = 13), 6.93 ± 0.220 (*ARKabc-1*/ARKb-mNG OX, ±SEM, n = 36).

(B) Comparison of tip growth rates in the presence of 500 pM or 50 nM latrunculin A (LatA). The mCherry-α-tubulin line was used for drug treatment. The mean rate (µm/h) was 9.69 ± 1.20 (*ARKabc-1*, ±SEM, n = 5), 23.0 ± 1.00 (control [+0.5% DMSO], ±SEM, n = 5), 16.7 ± 1.20 (+500 pM LatA, ±SEM, n = 6), 9.64 ± 0.702 (+50 nM LatA, ± SEM, n = 17).

(C) Representative images and comparison of intensities of functional Rop4-mNG at the cell tip. Images were acquired using a spinning-disc confocal microscope with a z-series taken every 0.5 µm for a range of 15 µm. The best focal plane is presented. Scale bar: 5 µm. The mean intensity was 1.29 ± 0.0724 (control, ±SEM, n = 6), 1.54 ± 0.140 (*ARKabc-1*, ±SEM, n = 6).

(D) Representative images and comparison of intensities of Arp3a-mNG at the cell tip. Images were acquired using a spinning-disc confocal microscope with a z-series taken every 0.5 µm for a range of 15 µm. The best focal plane is presented. Scale bar: 5 µm. The mean intensity was 1.75 ± 0.0814 (control, ±SEM, n = 29), 0.726 ± 0.107 (*ARKabc-1*, ±SEM, n = 20). P-value was calculated using Student's two-sample t-test: P < 0.0000001 (*Control - ARKabc-1*).

(E) The apical accumulation of RopGEF3 and RopGEF6 depends on the microtubules. Snapshots of the same cell before and 50-min after oryzalin addition are shown. DMSO was used as a control. mCherry-α-tubulin-expressing RopGEF3-mNG or RopGEF6-mNG was used in this experiment. Images were acquired with a spinning-disc confocal microscope using a z-series taken every 1.5 µm for a range of 6 µm. The best focal plane is presented. Scale bar: 5 µm.

(F) Temporal changes in RopGEF3-mNG or RopGEF6-mNG intensity at the cell tip after drug addition. A decrease in localisation was observed after microtubule disruption with oryzalin. Intensities relative to those before drug treatment are plotted (±SEM, n = 6–13).

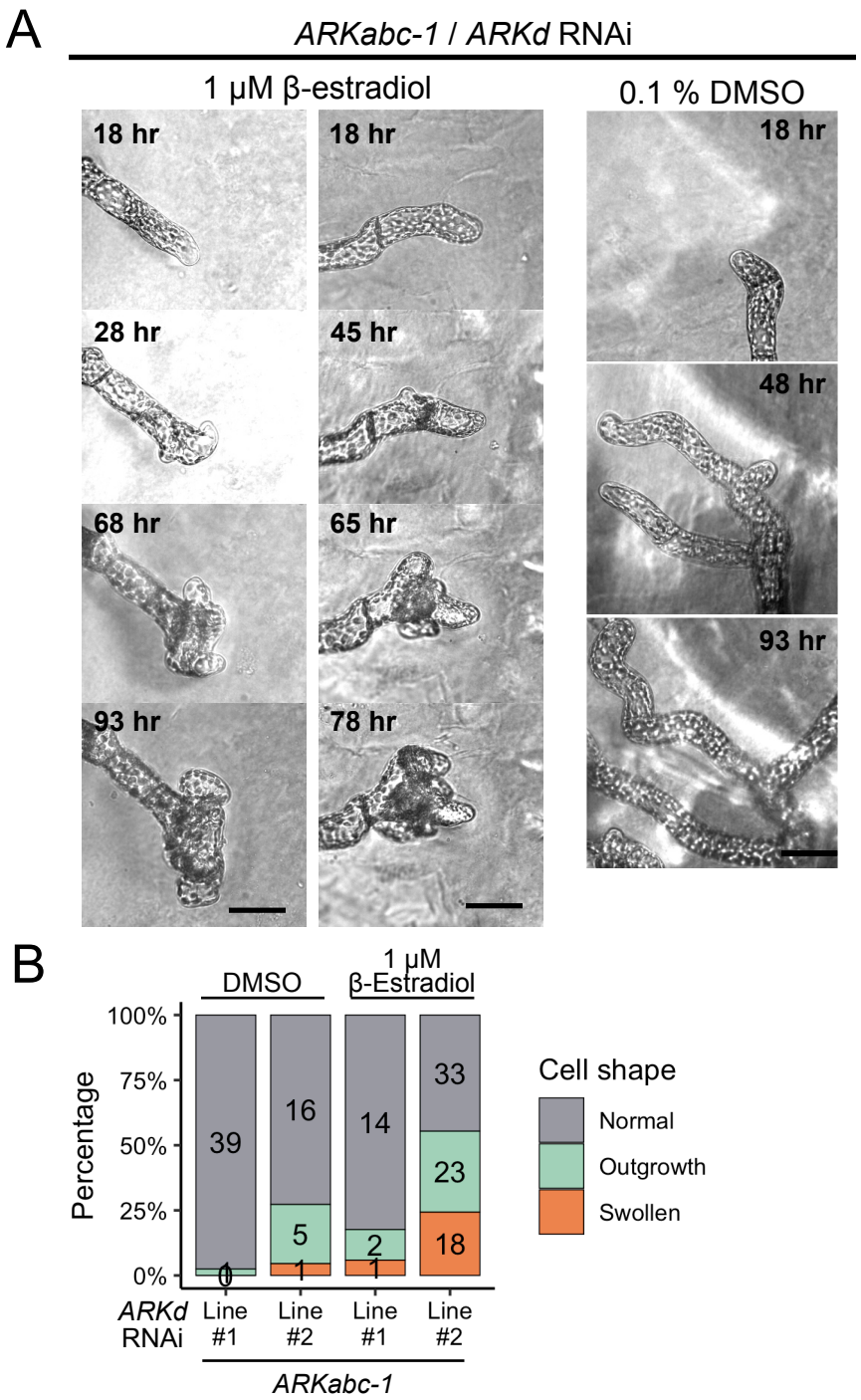

Supplemental Fig. 6 RNAi of *ARKd* in *ARKabc-1* causes abnormal outgrowth

(A) Representative image sequences of abnormal cell growth after *ARKd* RNAi induction by β-estradiol. Left, outgrowth in the apical cell; right, outgrowth in the subapical cell. Scale bars, 50 μm. Images were acquired using a wide-field microscope with transmission light.

(B) Comparison of apical cell shape after 1 μM β-estradiol or control 0.1% DMSO treatment. The numbers shown in the bar graphs indicate the actual number of counted cells.

S7

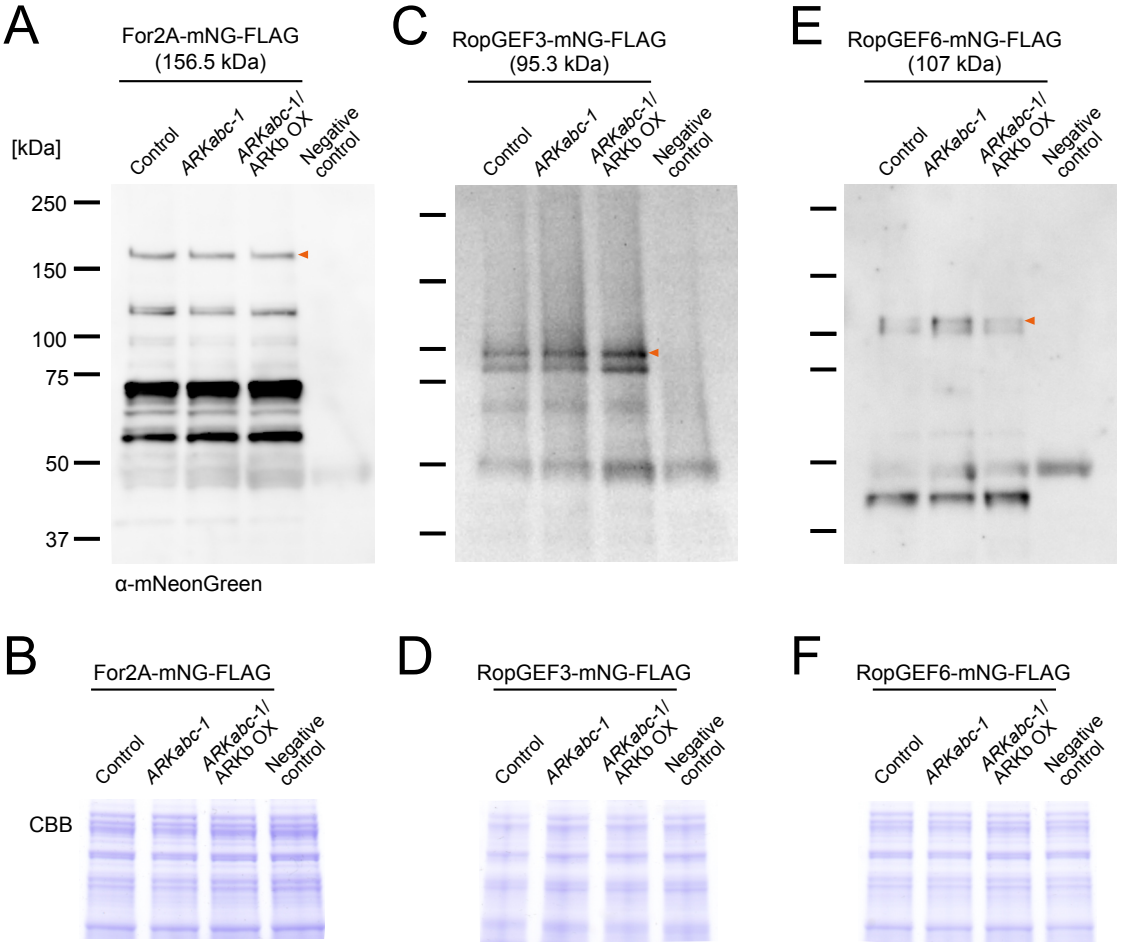

Supplemental Fig. 7 *ARK* deletion does not affect RopGEF or For2A expression level

(A), (C), and (E): Western blot following immunoprecipitation (IP). Anti-FLAG-conjugated magnetic agarose beads were used for IP, whereas anti-mNeonGreen antibody was used for western blotting. The negative control represents a moss line without mNG expression. Red arrows indicate the target protein size; smaller bands indicate degradation products or cross-reactions.

(B), (D), and (F): Loading control. The moss extracts used for IP were subjected to SDS-PAGE, followed by Coomassie Brilliant Blue staining.

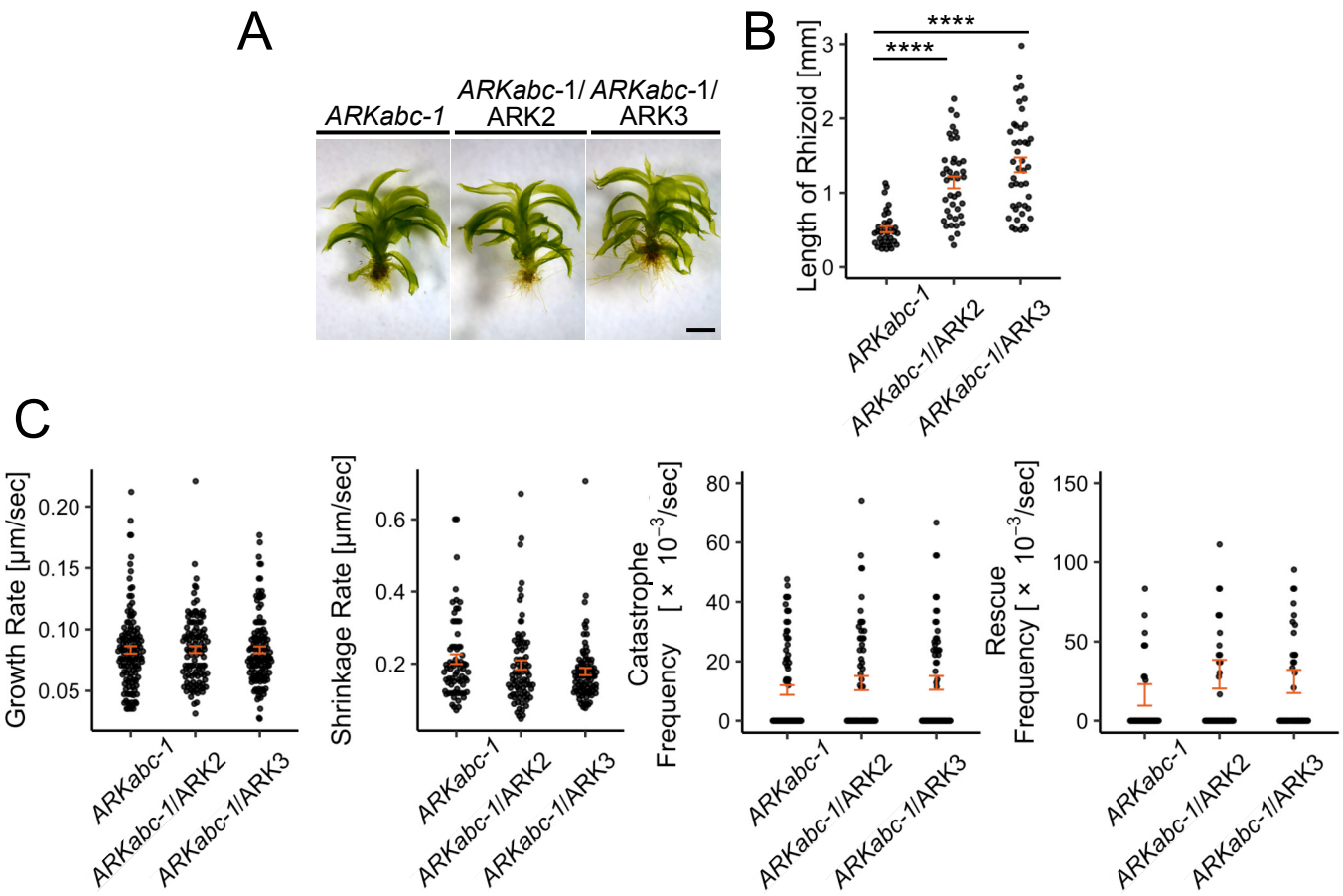

Supplemental Fig. 8 AtARK2 and AtARK3 expression rescued rhizoid development, but did not alter microtubule polymerisation dynamics

(A) Representative images of gametophores in the indicated lines. The image of the mutant line is identical to that presented in Fig. 1A. Scale bar: 1 mm.

(B) Rhizoid length comparison. The mean length (mm) was 0.510 ± 0.0406 (*ARKabc-1*, ±SEM, *n* = 34), 1.14 ± 0.0793 (*ARKabc-1*/ARK2-mNG OX, ±SEM, *n* = 41), 1.37 ± 0.0992 (*ARKabc-1*/ARK3-mNG OX, ±SEM, *n* = 43). The datasets of *ARKabc-1* are identical to those shown in Fig. S1D. P-values were calculated using the Steel-Dwass test: P = 0.00000003 (*ARKabc-1* - *ARKabc-1*/ARK2-mNG OX), P < 0.0000001 (*ARKabc-1* - *ARKabc-1*/ARK3-mNG OX).

(C) Comparison of microtubule polymerisation dynamics. The mean ± SEM, number of samples, and P-values are shown in Table S3.

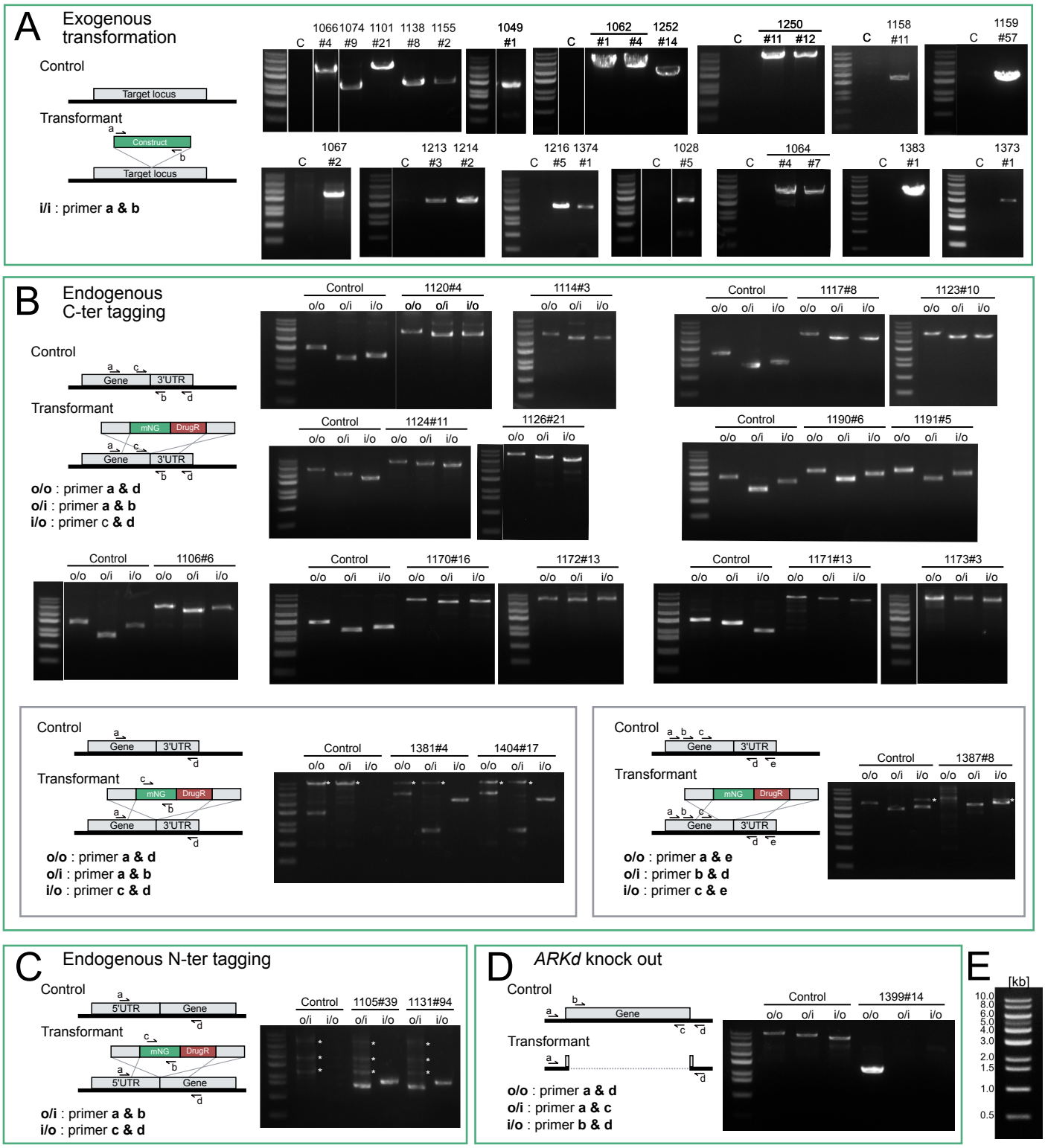

Supplemental Fig. 9 Confirmation of the moss lines established in this study
Genotyping PCR strategy (left) and PCR results (right) for the moss lines established in this study. (A) Exogenous integration, (B) C-terminal tagging, (C) N-terminal tagging, and (D) knockout. (E) Band-size markers used. Asterisks indicate non-specific bands. The number in each lane indicates the line ID, and the genotype of each ID is shown in Table S4. "C" indicates the control (parental line). Primers used are listed in Table S7.